Hydrogen ionization in 3d solar atmosphere models

Thomas Peter Golding

Thesis submitted for the degree of
Master of Astrophysics

Institute of Theoretical Astrophysics
University of Oslo

June 2010

Acknowledgments

Thank you Mats Carlsson and Jorrit Leenaarts for giving me a fun and some times quite frustrating master project, and for the help along the way. Thank you Mats for giving me a summer project working with Radyn and for sending me to summer school, both of which were fun and gave a decent learning outcome. Also thank you Viggo Hansteen for helping me getting the boundaries to run and with various other problems.

Thank you Kosovare for making me dinner when I was stressed out, thank you Håkon for eating lunch with me every day, thank you Eirik G. for reminding me why I shouldn't buy Apple products, thank you fellow students in the basement and thank you Lånekassen.

Contents

Chapter 1

Introduction

Simulations of the solar atmosphere began in the sixties when decent computing power started to become available. This enabled for complex, but time independent, physics to be addressed. The capacity of computers has since then grown, and solar simulations have become both time dependent and multi-dimensional. The codes of today provide valuable tools in the interpretation of modern observations.

Still, however, even the most advanced codes have to utilize simplifying assumptions and approximations in order for them to execute on reasonable time scales. The radiative transport of energy is especially difficult, making it the most relevant ingredient to simplify in a code. The equation of state is affected by this since occupation numbers (atomic level population numbers) depend on the radiation field. The proper treatment of the occupation numbers in a dynamic atmosphere includes keeping track of changes due to both advection and atomic transitions. This is very demanding in terms of computing power and computing time due to the non-local nature of the radiation field. It is common to assume local thermodynamic equilibrium (LTE), making the occupation numbers available through the well known equilibrium relations.

The instantaneous equilibration of thermodynamic quantities is not a very realistic assumption, especially in the chromosphere. Carlsson & Stein (2002) showed that the equilibration time for hydrogen ionization and recombination under chromospheric conditions range from 10^3-10^5 s except in shocks where it goes down due to an increase in temperature and mass density. They showed that this leads to a higher hydrogen ionization degree between shocks than predicted by LTE. As hydrogen is the most abundant element in stellar material, this greatly affects the electron density. The work of Carlsson & Stein (2002) was based on one-dimensional simulations

where the radiation field was treated in detail. Leenaarts & Wedemeyer-Böhm (2006) solved the hydrogen rate equations within the framework of the CO^{5}BOLD hydrodynamics code (Wedemeyer et al., 2004). This was made possible by an approximate treatment of the radiation field, developed by Sollum (1999). In Leenaarts & Wedemeyer-Böhm (2006) the state of the hydrogen did not couple back to the equation of state to partake in the determination of the hydrodynamics, but the results confirmed the general picture found in Carlsson & Stein (2002), showing similar electron densities. Leenaarts et al. (2007) studied the time dependent equation of state within the Oslo Stagger Code (Hansteen et al., 2007). They solved the rate equations for hydrogen in two dimensions with the same approximation as the one used in the 2006 paper, but also coupled this to the internal energy density of the system. They found that temperature fluctuations in the chromosphere are high and electron density fluctuations are low, due to a much more constant hydrogen ionization degree than what is given by LTE.

The OSC has in the last few years been rewritten. The new version (*Bifrost*) is a fully MPI parallel code that can run on large clusters with a distributed memory architecture (Gudiksen et al., 2010), thus enabling high resolution 3d models. Leenaarts' realistic equation of state was also transferred to the new code but was never properly debugged and tested and was as such not fully operational.

The focus of this work has been to bring Leenaarts' equation of state into a condition fit for production runs. The chapters 2 and 3 cover the underlying theory of magnetohydrodynamics and radiative transfer, chapter 4 outlines the strategy of solving the radiation magnetohydrodynamics equations numerically, in chapter 5 the hydrogen's special role is covered, in chapter 6 the code Bifrost is covered with special emphasis on Leenaarts' equation of state, in chapter 7 results of a three-dimensional simulation is presented, and finally in chapter 8 a conclusion and outlook is given.

Part I

Physics of the solar atmosphere

Chapter 2

Magnetohydrodynamics

When studying many-particle dynamics, if the mean free path of the particles is much shorter than the typical length scale of the phenomena under consideration, a continuum or fluid approach is justified. The mean free path is a measure of how far a particle is able to move between two successive interactions with neighbouring particles in which momentum is being transferred.

In this study of the solar atmosphere, the typical length scale is of the order of tens of kilometers. The mean free path in the atmosphere ranges from a few centimeters in the photosphere to a few kilometers in the corona, so the condition for a fluid approach is met, at least in the photosphere and chromosphere.

In section 2.1 a derivation of the equations governing a non-conducting fluid flow is given. From section 2.2 and out, the equations are generalized for a conducting fluid.

2.1 Hydrodynamics

Consider a volume, $\mathcal{V}$, with a surface $\mathcal{S}$ sitting fixed in a fluid flow $\mathbf{u}$ (figure 2.1). Let Q be a conserved quantity with density $q = \partial Q/\partial V$. The amount of Q contained within the volume $\mathcal{V}$ will change due to fluid flow transportation through the volume walls as well as due to quantity-dependent sources or sinks.

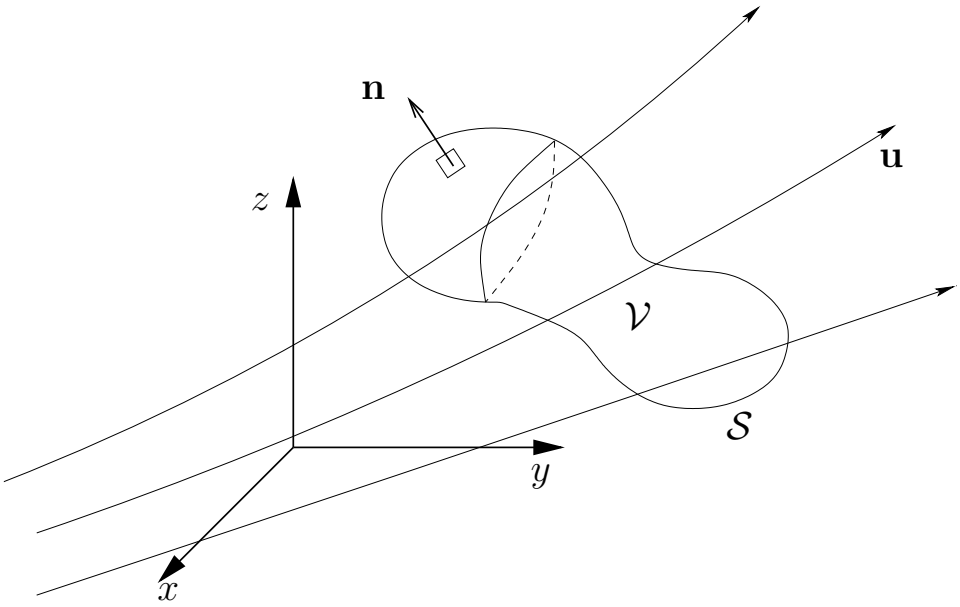

Figure 2.1: Fixed volume $\mathcal{V}$ with boundary surface $\mathcal{S}$ and surface element $d\mathbf{A} = \mathbf{n}\, dA$, where $\mathbf{n}$, is the surface unit normal, placed in a fluid flow $\mathbf{u}$.

2.1.1 Conservation of mass

Mass is a conserved quantity and its density is ρ. Consider the mass contained in the volume $\mathcal{V}$. It may only change due to the fluid flow transportation through the surface boundary,

$$\frac{d}{dt}\int_{\mathcal{V}} \rho\, dV \;=\; -\oint_{\mathcal{S}} \rho u_k n_k\, dA. \tag{2.1}$$

By the use of Gauss's integral theorem the surface integral may be transformed into a volume integral and one obtains the conservation of mass equation in differential form,

$$\frac{\partial \rho}{\partial t} \;=\; -\frac{\partial}{\partial x_k}\left(\rho u_k\right). \tag{2.2}$$

2.1.2 Conservation of momentum

Newton's second law states that a particle's change of momentum will be due to forces acting on it, $\sum F_i = dp_i/dt$. The total momentum contained

in the volume $\mathcal{V}$ will change due to the fluid flow transportation through the surface boundary and due to the various forces acting on it.

$$\frac{d}{dt}\int_{\mathcal{V}} \rho u_i \, dV = -\oint_{\mathcal{S}} (\rho u_i) u_k n_k \, dA + \oint_{\mathcal{S}} P_{ik} n_k \, dA + \int_{\mathcal{V}} \rho g_i \, dV, \quad (2.3)$$

where P_{ik} is the force per unit area acting on the inside from the outside of the volume in the i-th direction across a face whose normal is oriented in the k-th direction and g_i is the i-th component of the gravitation. By transforming all surface integrals into volume integrals, the differential form of the equation is found,

$$\frac{\partial}{\partial t}(\rho u_i) = -\frac{\partial}{\partial x_k}(\rho u_i u_k) + \frac{\partial}{\partial x_k}(P_{ik}) + \rho g_i. \quad (2.4)$$

P_{ij} - pressure and viscous stress

P_{ij} can be split into two parts, $P_{ij} = -p\delta_{ij} + \pi_{ij}$, where p is the thermodynamic pressure, δ_{ij} is the Kronecker delta function and π_{ij} is the viscous stress tensor. The viscous stress tensor is usually associated with the velocity gradient, see e.g. Mihalas & Mihalas (1984).

2.1.3 Conservation of energy

Energy is never destroyed, it only changes from one form to another. This means that,

$$\frac{d}{dt}\int_{\mathcal{V}} \mathcal{E} \, dV = - \oint_{\mathcal{S}} \mathcal{E} u_k n_k \, dS + \oint_{\mathcal{S}} u_i P_{ik} n_k dA + \oint_{\mathcal{S}} F_k^c n_k dA + \oint_{\mathcal{S}} F_k^r n_k dA, \quad (2.5)$$

where $\mathcal{E}$ is the energy density of the fluid, both kinetic and internal, $\mathcal{E} = \rho u_k u_k/2 + \rho\epsilon$. The first term on the right hand side represents the energy being transported through the surface boundary by fluid flow, the second term represents the viscous work (friction) and the work done on the surroundings due to expansion or contraction of the fluid, the third term represents the heat conduction and the fourth term represents the transport of energy through radiation. The energy flux due to heat conduction is proportional to the temperature gradient, $\mathbf{F}_c = -K\nabla T$, where K is a constant (F_k^c are the components of $\mathbf{F}_c$). This is known as Fourier's law. Radiative transfer is covered in chapter 3.

By the usual integral transformation one obtains the differential form of the energy equation,

$$\frac{\partial \mathcal{E}}{\partial t} = -\frac{\partial}{\partial x_k}(\mathcal{E}u_k) + \frac{\partial}{\partial x_k}(u_i P_{ik}) + \frac{\partial}{\partial x_k}(F_k^c + F_k^r). \tag{2.6}$$

2.2 Conducting fluid

If the temperature reaches certain heights, the particles making up the fluid will become charged due to ionization, and it will become a conducting fluid or a plasma. In this situation electromagnetic forces come into play, altering the equations of hydrodynamics. There will be an extra force term in the momentum equation (2.3) corresponding to the Lorentz force and an extra heating term in the energy equation (2.5) corresponding to ohmic heating.

2.2.1 Lorentz force term in momentum equation

In a multi-component fluid the electron density n_e is given by

$$n_e = \sum_{k,j} j n_{j,k}, \tag{2.7}$$

where $n_{i,j}$ is the number density of species i in ionization stage j (charge neutrality is assumed). The m-th component of the Lorentz force acting on the volume $\mathcal{V}$ (figure 2.1) where $\mathbf{E}$ and $\mathbf{B}$ are the electric and magnetic field, respectively, then takes the form

$$\begin{aligned} L_m &= \int_{\mathcal{V}} e\Big((\sum_{k,j} (j n_{j,k}(E_m + (\mathbf{u}_{j,k} \times \mathbf{B})_m)) - n_e(E_m + (\mathbf{u}_e \times \mathbf{B})_m) \Big)\, dV \\ &= \int_{\mathcal{V}} e\Big\{ (\sum_{k,j} j n_{j,k} - n_e) E_m + \Big((\sum_{k,j} j n_{j,k} \mathbf{u}_{j,k} - n_e \mathbf{u}_e) \times \mathbf{B} \Big)_m \Big\}\, dV \\ &= \int_{\mathcal{V}} ((\mathbf{j}_{ion} + \mathbf{j}_e) \times \mathbf{B})_m \, dV \\ &= \int_{\mathcal{V}} (\mathbf{j} \times \mathbf{B})_m \, dV, \end{aligned} \tag{2.8}$$

where e is the electron charge, $\mathbf{u}_{j,k}$ is the velocity of the k-th species in the j-th stage of ionization, $\mathbf{u}_e$ is the velocity of the electrons, $\mathbf{j}_{ion}$ is the ion current density, $\mathbf{j}_e$ is the electron current density and finally $\mathbf{j} = \mathbf{j}_{ion} + \mathbf{j}_e$ is the total current density. The term associated with the electric field falls out due to the assumption of charge neutrality.

2.2.2 Current density

Define

$$n_{ion} = \sum_{k,j} n_{j,k}, \tag{2.9}$$

$$Z = \frac{\sum_{k,j} j n_{j,k}}{n_{ion}} \quad \text{and} \tag{2.10}$$

$$\mathbf{u}_{ion} = \frac{\sum_{k,j} j n_{j,k} \mathbf{u}_{j,k}}{Z n_{ion}}, \tag{2.11}$$

where n_{ion} is the total ion density, Z is the mean ionization stage and $\mathbf{u}_{ion}$ is the mean ion velocity. With these definitions the current density takes the form

$$\begin{aligned} \mathbf{j} &= e(n_{ion} Z \mathbf{u}_{ion} - n_e \mathbf{u}_e) \\ &= -e n_e (\mathbf{u}_e - \mathbf{u}_{ion}) \\ &= -e n_e \mathbf{u'}_e, \end{aligned} \tag{2.12}$$

where $\mathbf{u'}_e = \mathbf{u}_e - \mathbf{u}_{ion}$ is the electron velocity in the rest frame of the ions and the charge neutrality condition (eq. 2.7) was used to eliminate the ion charge density. By identifying this as a Galilean transformation to the rest frame of the ions, it is clear that the electron current density in the ion rest frame is the same as the current density in the laboratory frame, $\mathbf{j'}_e = \mathbf{j}$.

The electron current density in the ion rest frame, $\mathbf{j'}_e$, can, according to Ohm's law, be expressed

$$\mathbf{j'}_e = \sigma \mathbf{E'}, \tag{2.13}$$

where σ is the conductivity. In the absence of strong spatial gradients in the magnetic field strength, the conductivity can be expressed as $\sigma = n_e e^2 / m_e \nu_c$, where m_e is the electron mass and ν_c is the mean collisional frequency associated with momentum transfer between the electrons and ions (see Shu, 1992, page 294).

2.2.3 Ohmic heating term in energy equation

The electron inertia is very small compared to the general ion inertia, and it will thus carry the vast majority of current in the fluid. The large inertia of the ions make them hard to move and they are therefore approximated to be in sync with the fluid flow, $\mathbf{u}_{ion} = \mathbf{u}$.

Consider the work, $dW = \mathbf{F}\cdot d\mathbf{x}$, done on the electrons by the electromagnetic force in the ion rest frame,

$$\begin{aligned} dW &= -en_e(\mathbf{E}' + \mathbf{u}'_e \times \mathbf{B}') \cdot \mathbf{u}'_e \, dV dt \\ &= \mathbf{j}'_e \cdot \mathbf{E}' dV dt. \end{aligned} \tag{2.14}$$

By combining this result with Ohm's law (eq. 2.13) and the fact that the electron current density in the ion rest frame equals the current density in the laboratory frame, the work done by the electromagnetic forces can be expressed as

$$dW = \frac{\mathbf{j}^2}{\sigma} dV dt, \tag{2.15}$$

and hence the ohmic heating term to appear in the energy equation 2.5 is

$$\int_{\mathcal{V}} \frac{\mathbf{j}^2}{\sigma} dV. \tag{2.16}$$

2.2.4 Induction equation

What remains now is to determine the evolution of the magnetic field, $\mathbf{B}$. Maxwell's equations are given by

$$\nabla \cdot \mathbf{E} = \frac{\rho_e}{\epsilon_0}, \tag{2.17}$$

$$\nabla \times \mathbf{E} = -\frac{\partial \mathbf{B}}{\partial t}, \tag{2.18}$$

$$\nabla \cdot \mathbf{B} = 0 \quad \text{and} \tag{2.19}$$

$$\nabla \times \mathbf{B} = \mu_0 \mathbf{j} + \mu_o \epsilon_0 \frac{\partial \mathbf{E}}{\partial t}, \tag{2.20}$$

where ρ_e is the total charge density and μ_0 and ϵ_0 are the permeability of free space and permittivity of free space, respectively. The last term in equation 2.20, containing the time derivative, may in the non-relativistic case safely be set to zero. By letting l_0 and t_0 represent the typical length- and timescale of the system one finds that this term is proportional to $l_0^2/t_0^2c^2 \sim v^2/c^2$.

In the non-relativistic limit the electromagnetic fields transform between reference frames,

$$\mathbf{B}' = \mathbf{B} \quad \text{and} \tag{2.21}$$

$$\mathbf{E}' = \mathbf{E} + \mathbf{u} \times \mathbf{B}. \tag{2.22}$$

Since $\mathbf{j}'_e = \mathbf{j}$ and $\mathbf{u}_{ion} = \mathbf{u}$, the current density is $\mathbf{j} = \sigma\mathbf{E}' = \sigma(\mathbf{E} + \mathbf{u} \times \mathbf{B})$. Isolating $\mathbf{E}$ gives $\mathbf{E} = \mathbf{j}/\sigma - \mathbf{u} \times \mathbf{B}$. Inserting this into eq. 2.18, and eliminating $\mathbf{j}$ by eq. 2.20 gives

$$\frac{\partial \mathbf{B}}{\partial t} = \nabla \times (\mathbf{u} \times \mathbf{B}) - \nabla \times (\eta \nabla \times \mathbf{B}), \tag{2.23}$$

where $\eta = (\sigma\mu_0)^{-1}$ is the resistivity. This is known as the induction equation.

2.2.5 Heat conduction

The description of heat conduction changes when the material is ionized. Fourier's law given in section 2.1.3, $\mathbf{F}^c = K\nabla T$, no longer holds. On a microscopic scale the transfer of energy by conduction is due to neighbouring particles colliding and exchanging momentum with each other. The nature of these processes change when particles carry an electric charge, and it is found that the energy flux in this case is

$$\mathbf{F}_c = \kappa_0 T^{5/2} \nabla T, \tag{2.24}$$

where κ_0 is a constant. See Spitzer (1967) for further details.

2.2.6 Magnetic pressure and plasma beta

The Lorentz force in the momentum conservation equation (eq. 2.8) can be decomposed:

$$\begin{aligned} \mathbf{L} = \mathbf{j} \times \mathbf{B} &= \frac{1}{\mu_0} (\nabla \times \mathbf{B}) \times \mathbf{B} \\ &= \frac{1}{\mu_0} (\nabla \cdot \mathbf{B}) - \frac{1}{2\mu_0} \nabla \mathbf{B}^2. \end{aligned} \tag{2.25}$$

The second term can be teamed together with the pressure in the momentum equation,

$$\begin{aligned} \frac{\partial \rho \mathbf{u}}{\partial t} &= -\nabla \left(p + \frac{\mathbf{B}^2}{2\mu_0} \right) + \dots \\ &= -\nabla \left[\frac{\mathbf{B}^2}{2\mu_0} (\beta + 1) \right] + \dots \end{aligned} \tag{2.26}$$

where the term $\mathbf{B}^2/2\mu_0$ is commonly referred to as the magnetic pressure, and β, known as the plasma beta parameter, is the ratio of gas pressure to magnetic pressure.

2.3 Summary

Stated below are the equations of hydrodynamics modified for the conducting fluid, known as the magnetohydrodynamic equations expressed in differential vector form:

$$\frac{\partial \rho}{\partial t} = -\nabla \cdot (\rho \mathbf{u}) \tag{2.27}$$

$$\frac{\partial \rho \mathbf{u}}{\partial t} = -\nabla \cdot (\rho \mathbf{u}\mathbf{u}) - \nabla p + \nabla \cdot \pi + \rho \mathbf{g} + \frac{1}{\mu_0}(\nabla \times \mathbf{B}) \times \mathbf{B} \tag{2.28}$$

$$\frac{\partial \mathcal{E}}{\partial t} = -\nabla \cdot (\mathcal{E}\mathbf{u}) + \frac{\partial}{\partial x_k}(u_i P_{ik}) + \nabla \cdot (\mathbf{F}_c + \mathbf{F}_r) + \eta \mu_0 \mathbf{j}^2 \tag{2.29}$$

$$\frac{\partial \mathbf{B}}{\partial t} = \nabla \times (\mathbf{u} \times \mathbf{B}) - \nabla \times (\eta \nabla \times \mathbf{B}) \tag{2.30}$$

2.4 Equation of state

The above eight equations (eq. 2.27, 2.28, 2.29 and 2.30) contain ten variables: the mass density, the energy density, the three components of the velocity, the three components of the magnetic field, the pressure and the temperature. In order to close the system, two more relations are needed. These are the pressure equation and the expression for the internal energy density ($\rho\varepsilon$),

$$p = kT(\sum_k n_k + n_e) \tag{2.31}$$

$$\begin{aligned} \rho\epsilon = {} & \frac{1}{2}kT(\sum_{k,j} f_k n_{j,k} + 3n_e) \\ & + \sum_k (\sum_j (\chi_{j,k} n_{j,k} + \sum_i \chi_{i,j,k} n_{i,j,k})) \\ & + \sum_{k=\text{molecules}} \xi_k n_k, \end{aligned} \tag{2.32}$$

where $n_{i,j,k}$ is the number density of the i-th excited state of the j-th ionization stage of the k-th species, $n_{j,k}$ is the number density of the j-th ionization stage of the k-th species, n_k is the number density of the k-th species, f_k is the number of degrees of freedom for the k-th species, $\chi_{i,j,k}$ is the excitation energy of the i-th excited state of the j-th stage of ionization of the k-th species, $\chi_{j,k}$ is the energy required to ionize species k from the $(j-1)$-th to the j-th stage of ionization and finally ξ_k is the dissociation energy of (molecule) species k. Energies of the different levels of excitation

and ionization of the species are found from atomic physics and are available in online tables such as TOP (Cunto et al., 1993) or NIST[1].

In equations 2.31 and 2.32 new variables are introduced. These are $n_{i,j,k}$, $n_{j,k}$, n_k and n_e. In order to determine them one can do one of two things: make an assumption or treat exact. How to perform the exact treatment is covered in chapter 3. In the next section the classic local thermodynamic equilibrium (LTE) assumption is covered.

2.4.1 Local thermodynamic equilibrium (LTE)

A closed system of particles is said to be in thermodynamic equilibrium (TE) if its thermodynamic variables no longer change in time. This corresponds to a situation where the particles have exchanged information through collisions for a time, τ_e, long enough to have come to an agreement on a state to collectively occupy. τ_e is often referred to as the *equilibration time*. When in TE, the system will be totally determined by two thermodynamic variables and the following relations are valid:

- Maxwell's velocity distribution for a particle species k with mass m_k,

$$n_k(v)\,dv = n_k \left(\frac{m_k}{2\pi kT}\right)^{3/2} e^{-m_k v^2/2kT} 4\pi v^2\,dv. \tag{2.33}$$

- Boltzmann's excitation equation relating the two excitation levels $n_{i,j,k}$ and $n_{l,j,k}$ with statistical weights $g_{i,j,k}$ and $g_{l,j,k}$,

$$\frac{n_{i,j,k}}{n_{l,j,k}} = \frac{g_{i,j,k}}{g_{l,j,k}} e^{-(\chi_{i,j,k}-\chi_{l,j,k})/kT}. \tag{2.34}$$

- Saha's equation

$$\frac{n_{i,j,k}}{n_{0,j+1,k}} = n_e \frac{g_{i,j,k}}{g_{0,j+1,k}} \left(\frac{h^2}{2\pi m_e kT}\right)^{3/2} e^{(\chi_{j+1,k}-\chi_{i,j,k})/kT}. \tag{2.35}$$

- A relation for the number densities of two successive stages of ionization,

$$\frac{n_{j,k}}{n_{j+1,k}} = n_e \frac{U_{j,k}(T)}{U_{j+1,k}(T)} \left(\frac{h^2}{2\pi m_e kT}\right)^{3/2} e^{\chi_{j+1,k}/kT}, \tag{2.36}$$

[1]National Institute of Standards and Technology, http://www.nist.gov/physlab/data/.

where $U_{j,k}$ is the partition function for the j-th ionization stage of the k-th species and is defined as

$$U_{j,k} = \sum_i g_{i,j,k} e^{-\chi_{i,j,k}/kT}. \tag{2.37}$$

Approximate analytical fits to the partition function of different elements, suitable for numeric work, are available in e.g. Cardona et al. (2010).

When assuming local thermodynamic equilibrium, one is effectively assuming that each point in the domain under consideration is a system of particles in thermodynamic equilibrium. The systems have an equilibration time, τ_e, which is infinitely small, i.e. they equilibrate to changes instantaneously and $n_{i,j,k}$, $n_{j,k}$, n_k and n_e are readily available by equations 2.34 and 2.35 if $T(\mathbf{r})$ and $\rho(\mathbf{r})$ are known (the mass density ρ gives the total number density of a species k once the gas composition is known).

Chapter 3

Radiative transfer

A star emits large amounts of radiative energy, all of which has to pass through its outer layers. The radiation is coupled to the matter and will therefore affect the gas dynamics. To properly model this coupling, extra terms must be added to the magneto-hydrodynamic equation set (2.27, 2.28, 2.29 and 2.30). The radiative effects that come into play are radiative pressure and radiative heating and cooling. When studying solar-like stars the radiative pressure is insignificant compared to the gas pressure and the magnetic pressure, hence it is left out of this text. The radiative heating and cooling is significant and a derivation of the term appearing in the energy equation (2.29) is given in section 3.2.

3.1 Specific intensity and the equation of transfer

The specific intensity is the primary quantity of radiative transfer. The energy emitted as radiation through a surface element dA with unit normal $\mathbf{n}$ in position $\mathbf{r}$ in the direction $\mathbf{s}$ in the frequency range $(\nu, \nu + d\nu)$ into a solid angle $d\Omega$ in a time interval dt is given as (see figure 3.1 for geometry)

$$dE_\nu = I(\mathbf{r}, \mathbf{s}, \nu, t) \cos\theta \, dA \, d\nu \, d\Omega \, dt, \tag{3.1}$$

where θ is the angle between $\mathbf{n}$ and $\mathbf{s}$. The constant of proportionality, $I(\mathbf{r}, \mathbf{s}, \nu, t)$, is defined as the specific intensity.

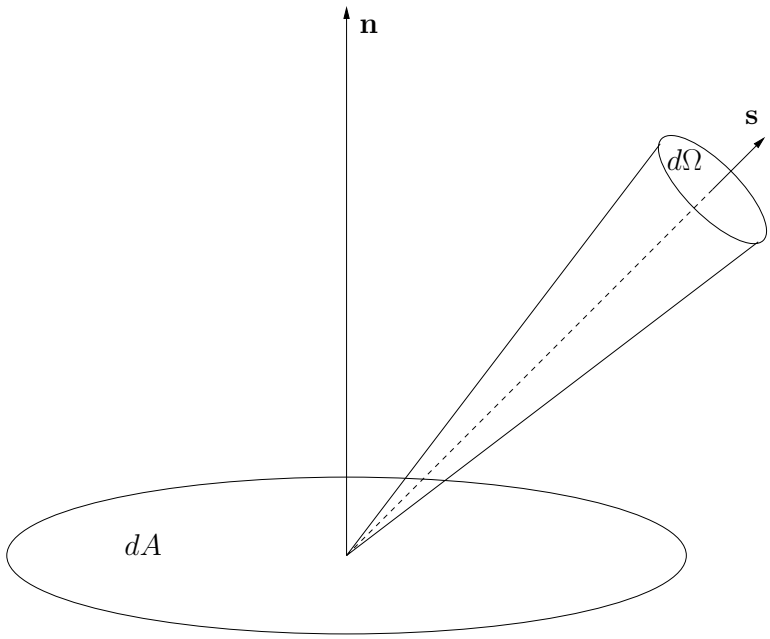

Figure 3.1: Specific intensity

3.1.1 Obtaining the specific intensity

Extinction coefficient

An element of material with cross-section dA and length ds will remove from a beam with specific intensity $I(\mathbf{r}, \mathbf{s}, \nu, t)$ propagating into a solid angle $d\Omega$ in a time interval dt an amount of energy

$$\delta E = \kappa(\mathbf{r}, \mathbf{s}, \nu, t) I(\mathbf{r}, \mathbf{s}, \nu, t)\, dA\, ds\, d\Omega\, d\nu\, dt, \tag{3.2}$$

where $\kappa(\mathbf{r}, \mathbf{s}, \nu, t)$ is defined as the extinction coefficient in the direction $\mathbf{s}$ for frequency ν at position $\mathbf{r}$ at time t.

Emission coefficient

An element of material with cross-section dA and length ds will release in direction $\mathbf{s}$ into a solid angle $d\Omega$ within a frequency range $(\nu, \nu + d\nu)$ in a time interval dt an amount of energy

$$\delta E = j(\mathbf{r}, \mathbf{s}, \nu, t)\, dA\, ds\, d\Omega\, d\nu\, dt, \tag{3.3}$$

where $j(\mathbf{r}, \mathbf{s}, \nu, t)$ is defined as the emission coefficient in position $\mathbf{r}$ in direction $\mathbf{s}$ for the frequency ν at time t.

Equation of transfer

The change in the amount of radiative energy travelling in direction $\mathbf{s}$ through a material element of cross-section dA and length ds into a solid angle $d\Omega$ in frequency range $(\nu, \nu + d\nu)$ in a time interval dt is

$$dI\, dA\, d\Omega\, d\nu\, dt = j\, dA\, ds\, d\Omega\, d\nu\, dt - \kappa I\, dA\, ds\, d\Omega\, d\nu\, dt, \tag{3.4}$$

where argument listing has been omitted for clarity. Also the cosine factor is not here since the beam is travelling along the normal of the cross-section area dA. Noting that

$$\begin{aligned} dI &= \frac{\partial I}{\partial t} dt + \frac{\partial I}{\partial s} ds \\ &= \left(\frac{1}{c} \frac{\partial}{\partial t} + \mathbf{s} \cdot \nabla \right) I\, ds, \end{aligned} \tag{3.5}$$

where c is the speed of light, it follows that

$$\left(\frac{1}{c} \frac{\partial}{\partial t} + \mathbf{s} \cdot \nabla \right) I = j - \kappa I, \tag{3.6}$$

which is formally known as the equation of transfer. Obtaining the specific intensity requires solving it. When working with a solar-like atmosphere, which is safely placed in the non-relativistic regime, the time dependent part can safely be left out. The equation is then reduced to,

$$\mathbf{s} \cdot \nabla_\tau I = S - I, \tag{3.7}$$

where $\nabla_\tau = \nabla / \kappa$ and S is the source function defined as $S = j/\kappa$.

3.2 Radiative heating

The radiation interacts with matter, either heating it or cooling it. This gives rise to a term in the energy equation (2.29). When the specific intensity is known, the flux can be obtained,

$$\mathbf{F}_r(\mathbf{r}, t) = \oint \mathbf{s} I(\mathbf{r}, \mathbf{s}, t)\, d\Omega. \tag{3.8}$$

Consider again the fluid element in figure 2.1. The heating rate of the element is

$$\begin{aligned} Q_r &= \oint_{\mathcal{S}} \mathbf{F}_r \cdot d\mathbf{A} \\ &= \int_{\mathcal{V}} \nabla \cdot \mathbf{F}_r\, dV. \end{aligned} \tag{3.9}$$

3.3 Matter in thermodynamic equilibrium

An introduction to TE and valid relations was given in section 2.4.1. Here a relation between the emissivity and extinction coefficients is added to the list.

- The Kirchhoff-Planck relation,

$$j = \kappa B, \tag{3.10}$$

where B is the Planck function,

$$B(T,\nu) = \frac{2h\nu^3}{c^2}\frac{1}{e^{h\nu/kT}-1}, \tag{3.11}$$

where h, c, k and T are Planck's constant, the speed of light, Boltzmann's constant and the temperature, respectively.

3.4 Atomic transitions

Contributions to the radiation field, both positive and negative, will be due to interaction between photons and the particles making up the medium they are travelling through. These particles are electrons, atoms, ions and molecules. The interactions include exchange of momentum between electrons and photons and energy transitions in the atoms releasing or removing a photon. The atoms can absorb a photon from the radiation field and use its energy to make a transition to a higher energy level or it can make a transition to a lower energy level and release a photon. The latter can happen either spontaneously or by the stimulation of a photon. Transitions involving a photon are referred to as *radiative* transitions. The transitions that are due to collisions between the particles making up the medium are referred to as *collisional* transitions.

3.4.1 Bound-bound radiative transitions

Einstein coefficients

The probability of a transition between two bound energy states in a quantum mechanical system, such as an atom, are given by the Einstein coefficients (see e.g. Griffiths, 1995) for the particular transition of the system

under consideration. There are three different types of transitions: spontaneous de-excitation, radiative (induced) de-excitation and radiative excitation corresponding to Einstein's A_{ji}, B_{ji} and B_{ij}, respectively.

A_{ji} is the probability of a spontaneous de-excitation from energy level j to the lower energy level i per unit time per atom residing in upper energy level j. $B_{ij}\overline{J}^{\phi}_{ij}$ is the probability of a radiative excitation from energy level i to energy level j per unit time per atom residing in the lower energy level i, where $\overline{J}^{\phi}_{ij}$ is the profile integrated mean intensity defined in equation 3.12. $B_{ji}\overline{J}^{\chi}_{ij}$ is the probability of a radiative or induced de-excitation from energy level j to energy level i per unit time per atom residing in the upper energy level j.

The profile integrated mean intensity is

$$\begin{aligned} \overline{J}^{f}_{ij} &= \int_0^\infty f(\nu-\nu_{ij})J\,d\nu \\ &= \int_0^\infty f(\nu-\nu_{ij})\frac{1}{4\pi}\oint I\,d\Omega\,d\nu, \end{aligned} \tag{3.12}$$

where f is the profile function of the transition between i and j, ν_{ij} is the photon frequency corresponding to the energy difference between the two energy levels, $E_j - E_i = h\nu_{ij}$ (h is Planck's constant). There are three different profile functions: ϕ, χ and ψ, corresponding to absorption, stimulated emission and spontaneous emission, respectively.

The Einstein coefficients are related, and the relations can be derived by assuming TE. When TE holds, transitions from the lower level, i, to the upper level, j, are expected to balance which means that

$$n_i B_{ij}\overline{J}^{\phi}_{ij} = n_j(A_{ji} + B_{ji}\overline{J}^{\chi}_{ji}), \tag{3.13}$$

where n_i and n_j are the population densities of the i and j energy level, respectively. Also (in TE) the profile integrated mean intensity, $\overline{J}^{f}_{ji}$, will be equal to the Planck function (eq. 3.11). This leads to the Einstein coefficient relations,

$$\frac{A_{ji}}{B_{ji}} = \frac{2h\nu_{ij}^3}{c^2} \tag{3.14}$$

$$\frac{B_{ij}}{B_{ji}} = \frac{g_j}{g_i}, \tag{3.15}$$

where g_i and g_j are the statistical weights (which the number of quantum mechanical states with the same energy) for the i-th and j-th energy level respectively. The TE relation, equation 2.34, is used to eliminate the occupation number ratio and exponential factors in eq. 3.15. Note that the Einstein coefficients are quantities depending on the atom alone, hence the relations above are valid also outside TE.

Line source function

The line emission coefficient and the line extinction corresponding to a transition between energy levels i and j are

$$j(\nu) = \frac{h\nu}{4\pi} n_j A_{ji} \psi \tag{3.16}$$

$$\kappa(\nu) = \frac{h\nu}{4\pi} \left(n_i B_{ij} \phi - n_j B_{ji} \chi \right), \tag{3.17}$$

hence the line source function is

$$S(\nu) = \frac{j}{\kappa} = \frac{2h\nu^3}{c^2} \frac{\psi}{\chi} \frac{1}{\frac{\psi}{\chi} \frac{g_j}{g_i} \frac{n_i}{n_j} - 1}. \tag{3.18}$$

The source function quickly reduces to the Planck function when complete redistribution (i.e. $\phi = \chi = \psi$) and TE holds.

3.4.2 Bound-free radiative transitions

Einstein-Milne relations

Analogs to the Einstein coefficients for the bound-bound transitions exist for bound-free transitions, and relations between these coefficients are called the Einstein-Milne relations. Let p_ν be the probability of a photoionization of an atom by a photon in the frequency range $(\nu,\ \nu + d\nu)$. p_ν is related to a photoionization cross-section, $\alpha = h\nu p_\nu$. For hydrogen (and other one-electron atoms and ions) this cross-section is given by Kramer's formula (Rutten, 2003)

$$\alpha_{ic}(\nu) = 2.815 \times 10^{29} \frac{Z^4}{i^5 \nu^3} g_{ic}, \tag{3.19}$$

where i is the bound level and principal quantum number, Z is the number of protons in the atom and g_{ic} is the Gaunt factor, a quantum mechanical correction factor of order unity. Now, armed with p_ν, the number of photoionizations from level i per unit time done by photons in the frequency range $(\nu,\ \nu + d\nu)$, $\partial n_{pi}/\partial t$, can be expressed

$$\frac{\partial n_{pi}(\nu)}{\partial t} = n_i p_\nu I_\nu \, d\nu, \tag{3.20}$$

where n_i is the number density of atoms residing in energy level i. The photon energy exceeding the ionization energy, χ_I, will be transferred into kinetic energy for the freed electron,

$$h\nu = \chi_I + \frac{m_e v^2}{2}. \tag{3.21}$$

Furthermore, let F and G be associated with the spontaneous and induced recombination probabilities, respectively, so that the total number of recombinations done by electrons in the velocity range $(v,\ v+dv)$ per unit time, $\partial n_{rec}/\partial t$, is

$$\frac{\partial n_{rec}(v)}{\partial t} = n_c n_e(v)[F + GI_\nu]v\,dv, \tag{3.22}$$

where n_c denotes the ion number density. n_{rec} might equally well be expressed as a frequency dependent quantity, by making use of the relation between v and ν given in equation 3.21. In TE the matter is in its most probable state, the number of photoionizations balance the number of recombinations and the specific intensity is equal to the Planck function (eq. 3.10), hence,

$$\begin{aligned} B(T,\nu) &= \frac{F}{G}\frac{1}{\frac{n_i p_\nu m_e}{n_c n_e(v) G h} - 1} \\ &= \frac{2h\nu^3}{c^2}\frac{1}{e^{h\nu/kT}-1}, \end{aligned} \tag{3.23}$$

giving rise to the Einstein-Milne relations for the continuum (by the help of eq. 2.33 and 2.35),

$$\frac{F}{G} = \frac{2h\nu^3}{c^2} \tag{3.24}$$

$$\frac{p_\nu}{G} = 8\pi v^2 \frac{g_c}{g_0}\left(\frac{m_e}{h}\right)^2. \tag{3.25}$$

Again, these relations depend only on the atom and are therefore also valid when the conditions for TE are not met.

Continuum source function

The continuum emission coefficient and the continuum extinction coefficient corresponding to a transition between energy level i and the continuum c are now obtainable:

$$\begin{aligned} j(\nu) &= h\nu\left(n_c n_e(v) F \frac{h}{m_e}\right) \\ &= n_c\left[\frac{n_i}{n_c}\right]^* \frac{2h\nu^3}{c^2} e^{-h\nu/kT}\alpha_{ic}(\nu), \end{aligned} \tag{3.26}$$

where $[n_i/n_c]^*$ is the TE ratio given in the Saha equation (eq. 2.35) and

$$\begin{aligned} \kappa(\nu) &= h\nu\left[n_i p_\nu - n_c n_e(v) G h/m_e\right] \\ &= \left(n_i - n_c\left[\frac{n_i}{n_c}\right]^* e^{-h\nu/kT}\right)\alpha_{ic}(\nu), \end{aligned} \tag{3.27}$$

This means that the source function becomes

$$S(\nu) = \frac{j}{\kappa} = \frac{2h\nu^3}{c^2} \frac{1}{\frac{n_i}{n_c[n_i/n_c]^*} e^{h\nu/kT} - 1}. \quad (3.28)$$

As was also found with the line source function (eq. 3.18), the continuum source function reduces to the Planck function (eq. 3.11) under TE conditions.

3.5 Free-free processes

Important free-free processes, such as *bremsstrahlung* and *Thomson scattering*, are treated in detail in standard literature ,e.g. Rybicki & Lightman (1986) and Shu (1991). In this text it suffices to say that emission and extinction are typically linear in the electron density. This is due to the nature of the processes - a photon and an electron interacting in some way.

3.6 Local thermodynamic equilibrium

Usually in radiative transfer problems, the temperature is allowed to vary (together with all other thermodynamic variables). This is also true in a stellar atmosphere, hence TE is not a valid approximation when solving such problems. However, one could let the TE relations be valid locally. For instance if the thermodynamic variables in the model are the temperature and mass density, then all the other thermodynamic variables, such as the occupation numbers, would be obtainable locally based on the local values of the temperature and mass density, thus giving the local emission and extinction coefficients, enabling the solution of the transfer equation. This approximation is referred to as local thermodynamic equilibrium or LTE.

By making the LTE assumption one is letting the matter reach its equilibrium state instantaneously - in other words, all particle-particle interaction happens on a timescale infinitesimally small. Unfortunately this is not the case in real life. A change in one variable will lead to a change in other variables as the particles interact with each other through collisions happening locally and it takes some time before the particles will agree on what state to collectively occupy. Matter's intricate coupling to the radiation field (i.e. absorption, photoionization, stimulated emission and stimulated recombination) lets the global state affect the local state. In order to increase the level of realism in the model, the LTE approach must be abandoned and non-local time dependent effects taken into account. Handling the radiative transfer in this more general case is the subject of section 3.7.

3.7 Time dependent non-LTE

The radiation field in a stellar atmosphere will affect the matter it is passing through and the matter will in turn affect the radiation field. The incoming radiative energy can be absorbed and hence exciting or ionizing the matter and the matter can de-excite or recombine, adding photons to the radiation field. Consistent treatment requires keeping close track of all the occupation numbers.

3.7.1 The rate equation

Consider figure 2.1 and let n_i denote the number density of the i-th excited level of a general atom. Then the rate of change of the total number of the atom's i-th excited level is

$$\begin{aligned} \frac{d}{dt}\int_{\mathcal{V}} n_i \, dV &= -\oint_{\mathcal{S}} n_i \mathbf{u}\cdot\mathbf{n}\, dA \\ &\quad + \int_{\mathcal{V}} \left(\sum_{j\neq i} n_j P_{ji} - n_i \sum_{j\neq i} P_{ij} \right) dV, \end{aligned} \tag{3.29}$$

where $\mathbf{u}$ is the velocity and P_{ij} is the number of transitions from the i-th to the j-th level per particle per unit time. By use making use of the divergence theorem, eq. 3.29 can be written,

$$\frac{\partial n_i}{\partial t} = -\nabla\cdot(n_i\mathbf{u}) + \sum_{j\neq i} n_j P_{ji} - n_i \sum_{j\neq i} P_{ij}. \tag{3.30}$$

The first term on the right is the advection term, the second is the rate term with transitions from all other levels to the i-th level and finally the third term is the rate term containing the transitions out of the i-th level.

3.7.2 Rate coefficients

The rate coefficients, P_{ij}, appearing in the rate equation (eq. 3.30) can be split in two parts. The first part is due to radiative transitions and the second one is due to collisions between the particles making up the gas, $P_{ij} = R_{ij} + C_{ij}$.

Radiative rate coefficients

In the bound-bound case, the radiative rate coefficients are given by the Einstein coefficients. The number of upward transitions from level i to level j is $B_{ij}\overline{J}^{\phi}_{ij}$ and the number of downward transitions is $A_{ji} + B_{ji}\overline{J}^{\chi}_{ij}$ (see section 3.4.1), hence the bound-bound radiative rate coefficients are

$$R_{ij} = B_{ij}\overline{J}^{\phi}_{ij} \tag{3.31}$$

$$R_{ji} = A_{ij} + B_{ij}\overline{J}^{\chi}_{ij} \tag{3.32}$$

In the bound-free case, the radiative rate coefficients are given by p_ν, F and G defined in section 3.4.2. The rate of photoionizations are found by integrating equation 3.20 over all frequencies. Likewise, the total number of recombinations is given by eliminating the v dependency in equation 3.22 by use of the Einstein-Milne relations (eq. 3.24 and 3.25) and integrating over all frequencies. The rate coefficients between the bound state i and the continuum c are then

$$R_{ic} = 4\pi \int_{\nu_{ic}}^{\infty} \frac{\sigma_{ic}(\nu)}{h\nu} J_\nu \, d\nu \tag{3.33}$$

$$R_{ci} = 4\pi \left[\frac{n_i}{n_c}\right]^* \int_{\nu_{ic}}^{\infty} \frac{\sigma_{ic}(\nu)}{h\nu} \left(\frac{2h\nu^3}{c^2} + J_\nu\right) e^{-h\nu/kT} \, d\nu, \tag{3.34}$$

where ν_{ic} is the ionization threshold frequency from level i. The recombination rate coefficient consists of two terms corresponding to spontaneous and induced recombination, respectively.

Collisional rate coefficients

The electrons, atoms, ions and molecules making up the gas in a stellar atmosphere may very well collide causing energy level transitions. The probability of a collision is proportional to the flux of particles, and due to the fact that the electron mass is about one thousandth of the proton mass, the electron flux will be dominate and electron-atom collisions will be the most important collisional process (Mihalas, 1978, page 132).

The electron collisional rate coefficients used for this study are based on Johnson (1972). Other collisional processes are ignored.

Part II

Numerical modelling

Chapter 4

Radiation-MHD simulations

The interpretation of observations of the solar atmosphere must be done on the basis of theory. One way to go forward is to compare numerical simulations to observations, altering the conditions for which the simulation is to be carried out, hopefully being able to identify from this the physical processes and their relevance for various phenomena and ultimately quantify them.

By the spatial and temporal discretization of reality (i.e. the variables defining the state of the system) the equations governing the system (eq. 2.27, 2.28, 2.29, 2.30 and the appropriate equation of state and radiative transfer machinery) can be reduced to computer friendly form. Solving these new reduced equations with sensible boundary conditions provides the researcher with time series of the variables for exploration and analysis.

4.1 Simulations with no radiative transfer

Equation of state and radiative transfer problems set aside, the equations that are to be solved are partial differential equations. Typically they are of the form,

$$\frac{\partial y}{\partial t} = f_1(\mathbf{r}) + f_2(\mathbf{r}) + \ldots + f_n(\mathbf{r}), \tag{4.1}$$

where the right hand side terms (f_i) may contain spatial derivatives. The strategy is to compute the right hand side and advance the variables by numeric integration. This is fairly straight forward: spatial derivatives are

numerically obtained by local variable differences, $dy/dx \sim \Delta y/\Delta x$, and the time integration is in principle simple,

$$y(t + \Delta t) \approx y(t) + \frac{\partial y}{\partial t}\Delta t. \tag{4.2}$$

The problem is reduced to looping through the computational domain, compute and add up various spatial derivatives, perform time integration and repeat the above - quick and effective. Both spatial derivatives and time stepping procedures can be refined to higher orders of accuracy. The Bifrost code (chapter 6), for instance, uses sixth order derivative operators and a predictor-corrector setup for time stepping.

4.2 Simulations with radiative transfer

For physical systems where radiative transfer does not play an important physical role the above strategy is a good one. Unfortunately, difficulties arise when radiation is taken into account, such as it must in the solar atmosphere. While changes in the variables in the non-radiative case were characterized by the local spatial derivatives, and hence are locally determined, the radiation transfer couples to the matter in a global fashion. Heating and cooling of the material is dependent on the specific intensity (see section 3.2) which is found through the solution of the transfer equation (eq. 3.7). The solution of the transfer equation is basically the source function integrated over the whole atmosphere, and the source function is dependent on the occupation numbers. The occupation numbers are generally known through the solution of the rate equations (eq. 3.30).

The inclusion of detailed radiative transfer in solar atmospheric simulations without simplifying approximations is a very demanding task in terms of computing time. There is one rate equation per atomic state possible within the mixture of gas employed in the simulation. The rate coefficients are depending on local conditions as well as the mean intensity in enough frequencies to be able to solve the frequency integrals (section 3.7.2), and the mean intensity requires the knowledge of the specific intensity in enough angles to be able to solve the angle integral.

4.2.1 LTE, an extreme simplification

The general type of solar atmospheric simulations as described above has to date only been possible to perform in one spatial dimension (see e.g.

Carlsson & Stein, 1992, 1995, 1997, 2002). In three dimensions computing time exceeds present day computing power and simplifying assumptions are required. One important simplifying assumption is that the material state is fully determined locally, i.e. two thermodynamic variables (such as mass and energy density) provides all relevant thermodynamic information (which is the occupation numbers, pressure, temperature and electron density) through the LTE relations presented in section 2.4.1. No rate equations need solving and the source function is always equal to the Planck function, hence the solution of the transfer equation can be obtained at a far lower computational cost than it would in the general case.

In the next chapter it is shown that LTE is not a good assumption for chromospheric conditions and a refined approximation is presented.

Chapter 5

Non-equilibrium hydrogen ionization

The state variables link together in the equations of state (see section 2.4) through the occupation numbers. The evolution of the occupation numbers is determined from the rate equations (eq. 3.30) where changes occur due to the fluid flow and the collisional and radiative atomic transitions. In traditional modelling the occupation numbers are set to obey their equilibrium partitioning, known as the LTE assumption. In section 5.1 it is shown that hydrogen is not generally found to be in LTE and that the element completely dominates the equation of state. In section 5.2 a quasi realistic treatment of hydrogen is presented.

5.1 Hydrogen's important role

The degree of ionization in the solar atmosphere is important in setting the temperature, pressure and the extinction and emission coefficients. Of all the different elements composing the atmospheric material, hydrogen is the most important, accounting for about 90% of the atomic nuclei (e.g. Grevesse & Sauval, 1998). Being so abundant, its state should be monitored closely.

Electron density

Figure 5.1 explicitly displays the relative importance of hydrogen, helium and other metals in setting the electron density in solar material under LTE conditions. At temperatures below 5000 K, metals are the dominating

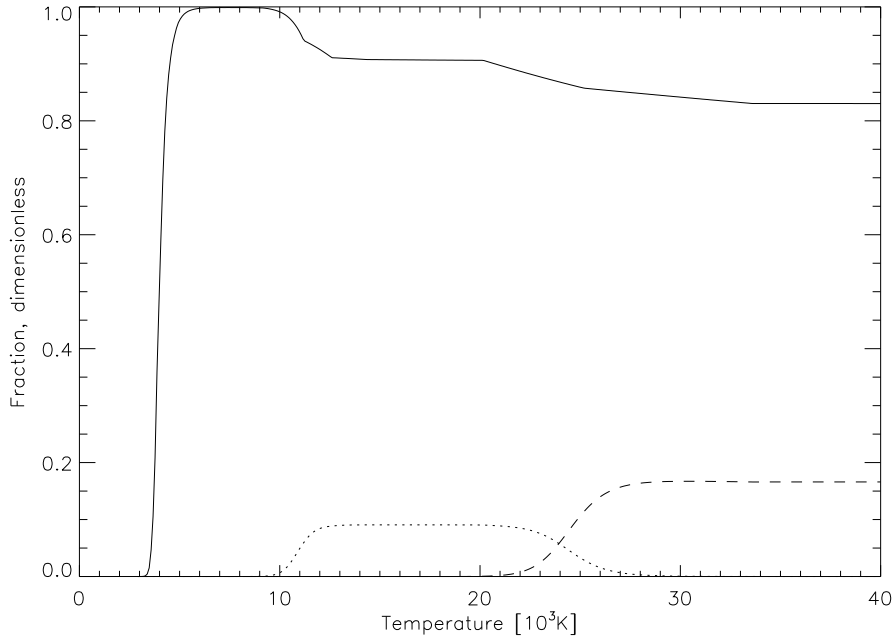

Figure 5.1: LTE electron contribution ratios, $jn_{j,k}/n_e$, in solar material. Shown here are H II (solid), He II (dotted) and He III (dashed). At low temperatures metals are the dominating electron contributors. In the temperature range $5000-10000$K hydrogen dominates. This dominance weakens as helium ionizes at temperatures above 10000K.

electron donor, while ionized hydrogen is the dominant contributor to the electron density above this point. From 10000 K and up, 10-20% of the electrons are coming from ionized helium. This is set into context in figure 5.2, showing various quantities for the Val3C model atmosphere (Vernazza et al., 1981). The upper panel shows the temperature- and mass density structure of the classic model. The middle panel shows the electron density and hydrogen ionization degree for two different scenarios: all elements in LTE and all elements in LTE but hydrogen which is in statistical equilibrium. The difference in ionization degree in SE and LTE is seen to have a serious impact on the electron density. The lower panel displays the relative importance of hydrogen (in both the SE and LTE case), helium and metals (both in LTE) in setting the electron density. From just above the temperature minimum, at 0.7 Mm, hydrogen is the dominant electron contributor. Below this height, the metals are providing the most electrons. Deep in the atmosphere, where the temperature rises, hydrogen is again being ionized and starts to dominate the contributions to the electron density.

Internal energy

The ionization degree plays an integral part of the energetics of the system. The internal energy density is given by (eq. 2.32)

$$\begin{aligned}\rho\epsilon &= \frac{1}{2}kT(\sum_{k,j} f_k n_{j,k} + 3n_e) \\ &\quad + \sum_k(\sum_j(\chi_{j,k}n_{j,k} + \sum_i \chi_{i,j,k}n_{i,j,k})) \\ &\quad + \sum_{k=\text{molecules}} \xi_k n_k,\end{aligned}$$

where the first term represents the thermal energy, the second term represents ionization and excitation energy and the third term represents molecule dissociation energy. Under solar atmospheric conditions molecule formation is mostly insignificant and the energy will mainly go into thermal motion (corresponding to the first term) or into ionizing and exciting the material (corresponding to the second term).

The contributions from the different terms in eq. 2.32 are displayed for the Val3C atmosphere in figure 5.3. All elements are treated in LTE except for hydrogen which is treated in both SE (upper panel) and LTE (lower panel). The internal energy is not the same for the two cases, but in the upper chromosphere the contribution due to hydrogen ionization is the dominant one in both the SE and the LTE case. At all other heights, the thermal energy term is the dominating one. In other words, the temperature in the

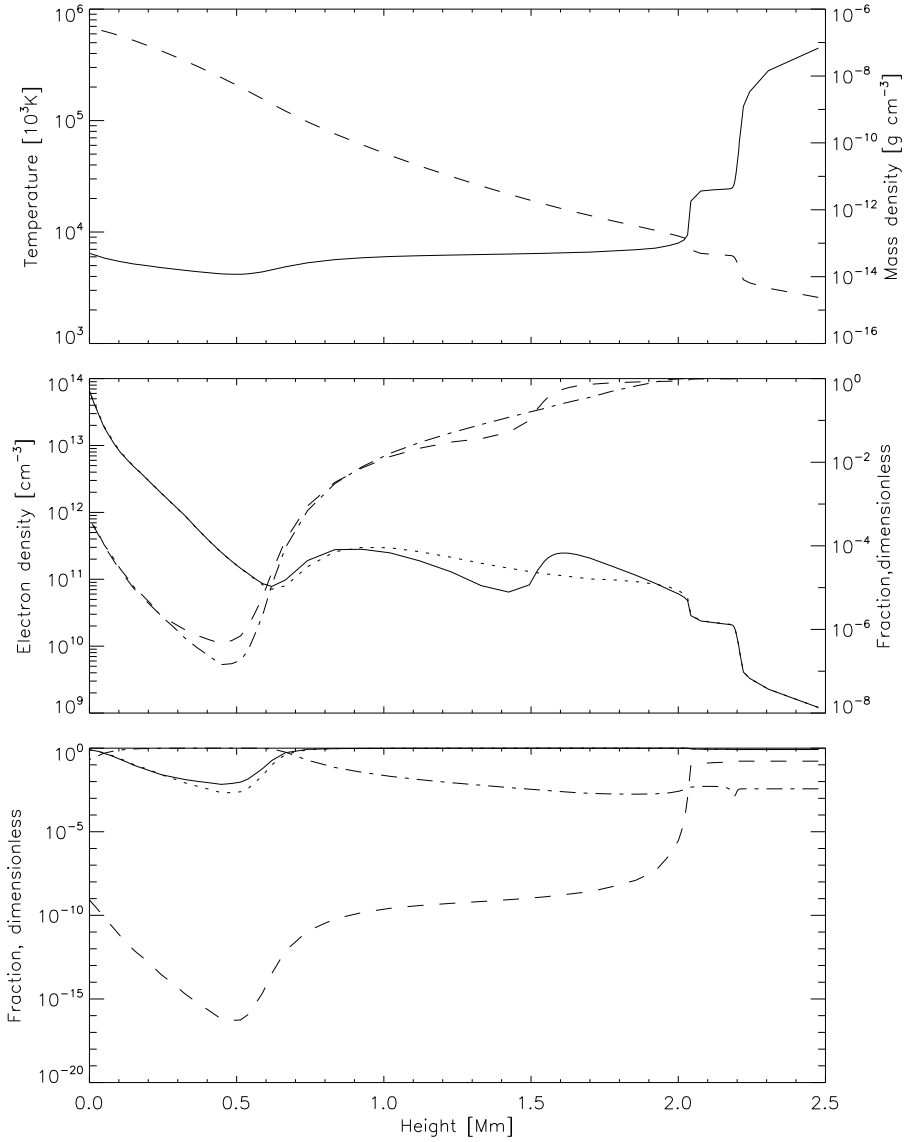

Figure 5.2: Various quantities of the Val3C model atmosphere. Upper panel: temperature (solid, scale to the left), mass density (dashed, scale to the right). Middle panel: electron density (scale to the left) where hydrogen is in statistical equilibrium (SE) and other elements in LTE (solid), where all elements are in LTE (dotted), ionization degree (scale to the right) of hydrogen in SE (dashed), of hydrogen in LTE (dashed-dotted). Lower panel: electron density contributions, $jn_{j,k}/n_e$, of hydrogen in SE (solid), of hydrogen in LTE (dotted), of helium in LTE (dashed), of all other elements in LTE (dashed-dotted).

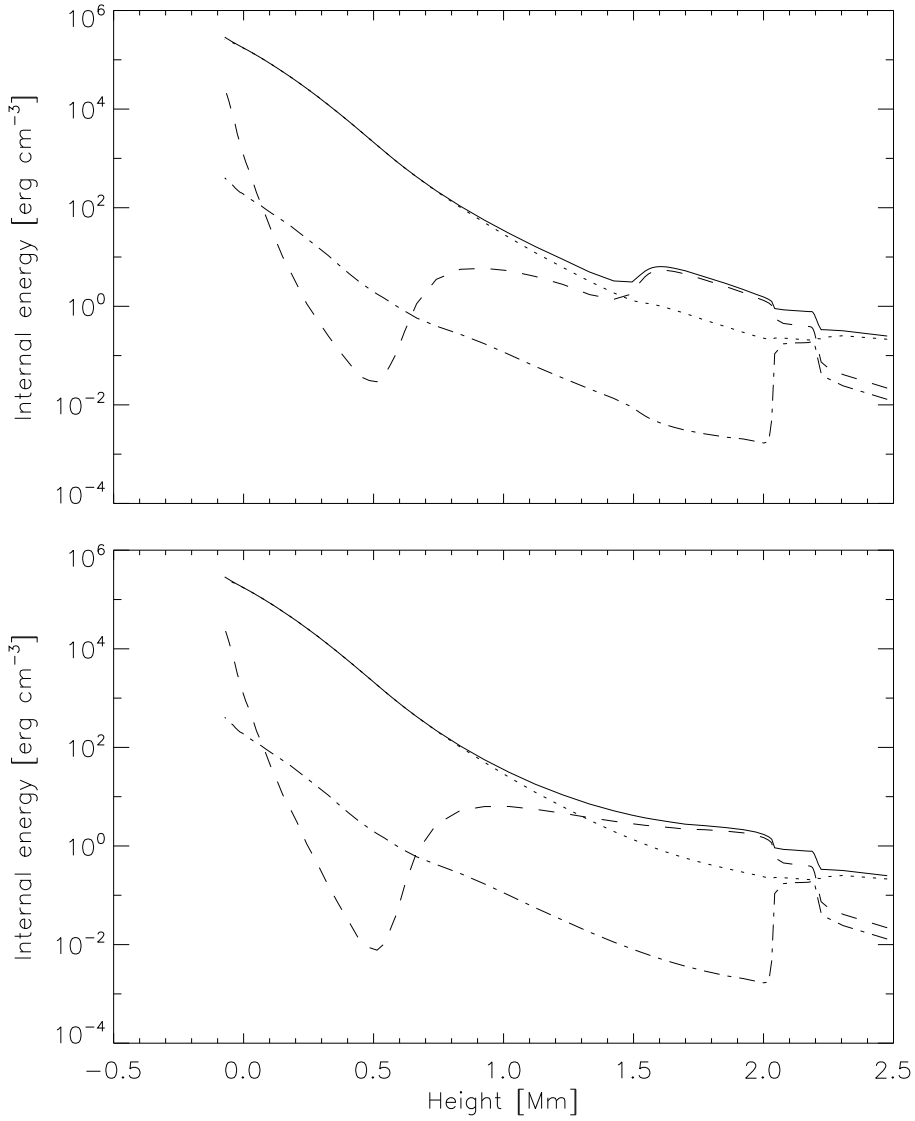

Figure 5.3: Energy contributions in the Val3C atmosphere. Upper panel: all elements in LTE but hydrogen which is in SE, lower panel: all elements in LTE. Total internal energy (solid), thermal contribution (dotted), ionization energy contribution due to hydrogen (dashed) and due to other elements (dashed-dotted).

upper chromosphere will be set by the hydrogen ionization degree. Larger levels of ionization causes the thermal motion term in eq. 2.32 to compensate, i.e. adjust the temperature down. When ionization levels are low, the temperature is adjusted up.

5.1.1 Dynamic atmosphere

Dynamic atmosphere models are different from the Val3C model presented above. The static picture is not, however, worthless, as it displays that the non-local effects (i.e. interaction of radiation field) will in general strive to produce a different ionization degree than predicted by the LTE assumption. Although only hydrogen was allowed to interact with the radiation field, it was seen to be the dominant term in the equation of state, hence insight is gained by treating it in a detailed fashion (solving its rate equations) even though all other elements are treated in LTE.

According to the one-dimensional dynamic atmosphere studies presented in Carlsson & Stein (1992, 2002), chromospheric shock wave structure differs significantly in the LTE and non-LTE case. This is due to the timescales of the rates. Equilibration time scales for the ionization and recombination are of the order $\sim 10^3$-10^5 s while the chromospheric state conditions change on timescales $\sim 10^2$ s. One consequence of these time scales is that hydrogen is ionized in shock fronts propagating through the chromosphere as temperature and density increase. The shocks pass through too frequently to let the hydrogen equilibrate to local conditions (which would not have been LTE, but SE). This means that between shocks, the ionization degree is higher than local conditions predict, hence there are more electrons and the temperature is lower as more of the internal energy is tied up in ionization (see fig. 5.3).

5.2 The Sollum approximation

Reducing the number of rate equations that are to be solved in the general case would save enormous amounts of computing time. For instance, granting hydrogen its importance, a good choice would be to only solve the rate equations for hydrogen and treat all other elements as if they were in LTE. As seen in section 5.1, hydrogen is dominating the equation of state, and therefore such an omission would give the best payoff in terms of realism per equation solved, resulting in a limited error in the description of important state variables such as temperature, pressure and electron density would only be. Nevertheless, the presence of the non-local component in the

rate equations (the mean intensity in the radiative rate coefficients) makes the exact solution of even this reduced set of rate equations impossible on today's computing facilities.

By approximating the mean radiation field, Espen Sollum found a way around this problem (Sollum, 1999). He recognized that the mean intensity in frequencies relevant for hydrogen transitions decouples from local conditions in the photosphere and remains approximately unchanged above this point. The consequence of this is that the rate equations for hydrogen become local and can be solved like the other MHD equations (see section 4.1).

5.2.1 Background

The radiation decoupling from local atmospheric conditions is displayed in figure 5.4. Statistical equilibrium is computed for a Radyn simulation snapshot (Carlsson & Stein, 1992) and the figure shows the gas temperature (solid), the radiation temperature of the Lyα line core (dotted) and the radiation temperature of the Balmer ionization edge (dashed). These two radiation temperatures illustrate nicely the two types of typical behavior of radiation in the hydrogen transitions in a solar-like atmosphere: decoupling in the photosphere and decoupling in the chromosphere. Investigation of all the possible line and continuum transitions (available in a model atom with a limited number of energy levels) shows that decoupling from local conditions happen in the photosphere except for Lyman transitions which have some coupling in the upper chromosphere. However, the Lyman transitions are to a good approximation found to be in detailed radiative balance ($n_i R_{ij} = n_j R_{ji}$) everywhere except for just below the transition region.

5.2.2 Approximation

The radiation field

The photons escaping the photosphere due to transitions in hydrogen interact very little with the gas travelling through the atmosphere. Since the photospheric density and temperature conditions have a slow rate of change, these photons make up a stable outgoing energy flux (see Balmer ionization edge in fig. 5.4). The stability of this flux makes it a good parameter choice when approximating the radiation field. Espen Sollum recognized this and he let the radiation temperature at the line core and ionization edge frequencies determine the approximated radiation field in a given model atmosphere

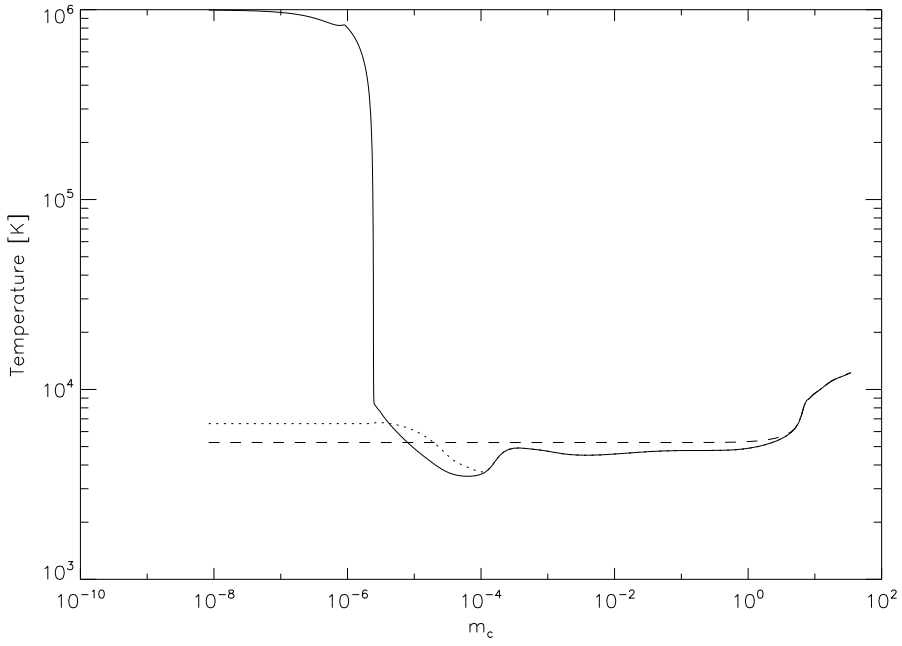

Figure 5.4: Various temperatures as functions of column mass. Temperature (solid), radiation temperature Lyα at line center (dotted) and radiation temperature Balmer continuum at ionization edge (dashed). The Balmer continuum is seen to decouple from atmospheric temperature in the photosphere. This implies that photons originating here are able to travel unhindered outward and ultimately escape. Coupling between atmosphere and Lyα photons is evident, and in the upper parts of the chromosphere, the radiation temperature rises above atmospheric temperature indicating non-LTE conditions where photons originating non-locally are present. Above the transition zone the atmosphere turns optically thin due to the fact that practically all hydrogen is ionized.

vertical column,

$$J_{ij}(\nu_{ij}, m_c) = \begin{cases} B(\nu_{ij}, T_{ij}) \left[1 + \left(\frac{m_c}{m_{crit}}\right)^{H_{ij}}\right] & \text{if } m_c < m_{crit} \\ B(\nu_{ij}, T(m_c)) & \text{if } m_c > m_{crit}, \end{cases} \quad (5.1)$$

where the subscript ij specifies the transition under consideration. B is the Planck function (eq. 3.11), T_{ij} is the radiation temperature input parameter corresponding to the observed average intensity in the line core or ionization edge of the transition ij, H_{ij} a parameter which Espen Sollum has determined for solar-like atmospheres (Sollum, 1999). m_c is the column mass,

$$m_c(z) = -\int_z^\infty \rho(z')\, dz', \quad (5.2)$$

and m_{crit}, the critical column mass, is the column mass at the lowermost height where $2B(\nu_{ij}, T_{ij}) = B(\nu_{ij}, T)$ is satisfied.

Radiative rate coefficients

By assuming that the mean intensity is frequency independent across the profile functions, the bound-bound radiative rate coefficients (eq. 3.31 and 3.32) are trivially obtained. The frequency integrals needed for the bound-free radiative rate coefficients (eq. 3.33 and 3.34) can be solved exactly when the radiation field is the Planck function (Sollum, 1999) and the cross section is given by Kramer's formula (eq. 3.19).

The Lyman transitions

The radiation field is found to be less predictable in the Lyman transitions (fig. 5.4) which complicates its a priori description. However, the Lyman transitions are found to be in detailed radiative balance in relevant parts of the atmosphere and the radiative rate coefficients going to or from the ground level can because of this all be set to zero in the rate equations.

Chapter 6

The Bifrost code

Bifrost is an MPI parallelized computer code that is set up to solve the magnetohydrodynamic equations (eq. 2.27, 2.28, 2.29 and 2.30) in Cartesian coordinates on a staggered grid using 5th order interpolation operators and 6th order derivative operators. The code includes heat conduction along the magnetic field lines (section 2.2.5) and solves the radiative flux divergence needed in the energy equation (section 3.2) (Hayek, 2008). Scattering is taken into account (Skartlien, 2000) and the frequency integral is handled by grouping together extinction coefficients based on their strength (Nordlund, 1982). The extinction coefficients are determined by assuming matter to be in LTE. The fundamental variables in the code are the three components of the momentum (p_x, p_y and p_z), the three components of the magnetic field (B_x, B_y and B_z) and the two thermodynamic variables mass density (ρ) and internal energy density ($\mathcal{E}$).

The boundaries are periodic on the lateral sides. In the top and bottom boundary, different setups are in use, including setting symmetric, antisymmetric and extrapolated values. These boundaries are governed by characteristic equations, enabling the separation of incoming and outgoing information (Thompson, 1987, 1990).

The code is based on the *Oslo Stagger Code* (Hansteen et al., 2007) for which the parallelization worked on a shared memory system, whereas Bifrost works on distributed memory systems, thus enabling more extensive simulations. The schematic grid setup for a distributed memory system is shown in figure 6.1. The white regions are the subdomains and together they make out the full computational domain. The grey regions are copies of the neighbouring points from the neighbouring core. The grey points are referred to as *ghoszones*. These are necessary to solve the equations properly in the subdomain boundaries, and the number of ghostzones are

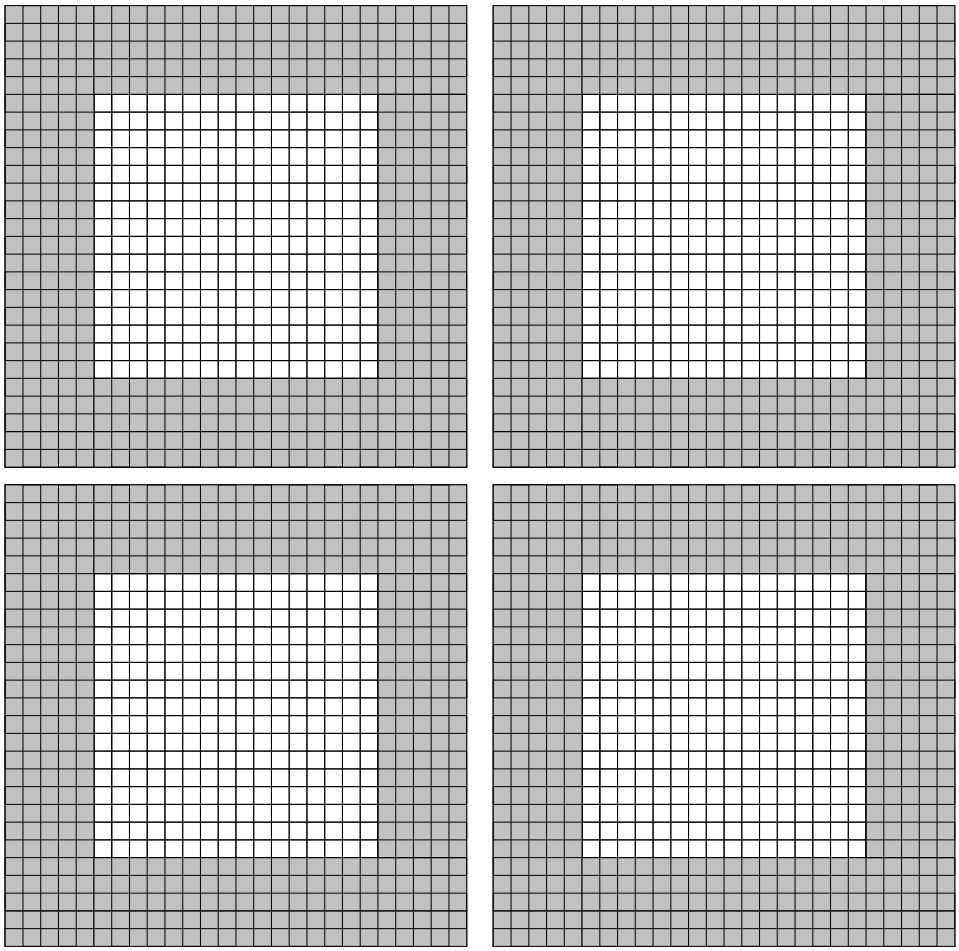

Figure 6.1: Schematic grid on a distributed memory system. Each of the squared represent one core, and the cores work on separated parts of the grid. Equations are solved in the white region. The grey points equal the neighbouring points in the neighbouring core and are necessary to work out derivatives, fluxes etc. The grey points are referred to as *ghostzones*.

dependent on which order is being used for the interpolation and derivative operators (i.e. how many neighbouring points needed to perform interpolation or compute a derivative). Every time the variables are updated (in the subdomains), ghostzone values must be communicated between the working cores to ensure a consistent solution along the subdomain boundaries.

With the exception of the numerical treatment of the equation of state found in the remainder of this chapter, more information on the code can be found in Gudiksen et al. (2010) and the references therein.

6.1 Equation of state

The code has three equation of state options, in order of increasing realism: perfect gas neglecting ionization, perfect gas with LTE ionization and perfect gas with LTE ionization except for hydrogen for which the rate equations are solved (time dependent non-LTE). The perfect gas with no internal degrees of freedom is mainly used for development purposes. The LTE option is the option used for most production runs. This option employs a precomputed table containing the gas pressure, the temperature, the electron density and the extinction coefficients for the various bins as functions of mass density and internal energy.

6.2 Time dependent non-LTE hydrogen treatment

In order to couple the time dependent state of hydrogen to the thermodynamics of the system, six new variables are introduced: the occupation numbers n_i, where $i = 1, 2, 3, 4, 5$, represents the five lowermost bound states of hydrogen and n_6 represents the number density of ionized hydrogen. Tracking the evolution of these new variables requires integration of the rate equations (eq. 3.30) and this is made possible by defining the radiation field prior to computation with the Sollum approximation. The rate equations are solved in two steps: first, the advection part, and second, the rate part. This technique is known as operator splitting (Press et al., 1992).

The occupation numbers couple to the temperature (T), the electron density (n_e) and the mass density (ρ) through the internal energy balance (eq. 2.32), charge conservation (eq. 2.7) and the conservation of hydrogen nuclei ($n_H^{tot} = A\rho$, where A is depending on the gas composition). It is thus necessary to solve eight extra equations. These equations are, in computer friendly form:

$$F_1 = 1 - \frac{n_6 + n_H^{tot} n_e^{noH}}{n_e} = 0 \tag{6.1}$$

$$F_2 = 1 - \frac{1}{e_i}\left\{\frac{3k_BT}{2}\left(n_e + n_H^{tot}n_{other}^{noH} + n_{H2} + \sum_{i=1}^{6} n_i\right) + n_H^{tot}e_i^{noH} + n_{H2}(\xi_{H2} + e_{H2}) + \sum_{i=1}^{6} n_i\chi_i\right\} = 0 \quad (6.2)$$

$$F_3 = 1 - \frac{1}{n_H^{tot}}\left(\sum_{i=1}^{6} n_i + 2n_{H2}\right) = 0 \quad (6.3)$$

$$F_{i'+3} = \frac{n_i}{n_i^{t_0}} - \frac{\Delta t}{n_i^{t_0}}\left(\sum_{j=1,j\neq i}^{6} n_j P_{ji} - n_i \sum_{j=1,j\neq i} P_{ij}\right) - 1 = 0, \quad (6.4)$$

where F_1, F_2 and F_3 represent the equation of charge conservation, energy conservation and hydrogen nuclei conservation, respectively. $F_{i'+3}$ represents 5 rate equations ($i' = 1, 2, 3, 4, 5$). The sixth rate equation is replaced by the hydrogen nuclei conservation equation to increase stability and convergence rate (see section 6.2.1) of the equation system (the rate equations become linearly dependent for statistical equilibrium). The new variables introduced here, $n_e^{noH} = n_e^{noH}(n_e, T)$, $e_i^{noH} = e_i^{noH}(n_e, T)$, n_{other}^{noH}, $n_{H2} = n_{H2}(n_i, T)$, $e_{H2} = e_{H2}(T)$ and ξ_{H2} correspond to the number density of electrons coming from elements other than hydrogen per hydrogen nuclei, the excitation and ionization energy of elements other than hydrogen per hydrogen nuclei, the number density of elements other than hydrogen per hydrogen nuclei, the number density of H_2 molecules, the internal energy (rotational and vibrational) per H_2 molecule and the dissipation energy of the H_2 molecule, respectively. n_e^{noH}, e_i^{noH} and n_{other}^{noH} are dependent on the gas composition, and their values are read from a precomputed table. n_{H2} and ξ_{H2} are determined from polynomial fits with coefficients found in Tsuji (1973) and Vardya (1965), respectively.

The above equations (eq. 6.1, 6.2, 6.3 and 6.4) are solved with the Newton-Raphson method explained in section 6.2.1.

Boundaries

At the lower boundary occupation numbers, and thereby temperature, electron density and pressure, are set to their LTE values consistent with the mass density and internal energy. These boundary conditions are justified since mass the density is high enough for non-local coupling due to radiation to be minimal.

At the upper boundary the advection is turned off and the rate equations (eq. 6.4) are solved as usual. Consistency with mass density is enforced through hydrogen nuclei conservation (eq. 6.3). Since the coronal equilibration time

is short (Carlsson & Stein, 2002) compared to its dynamics, this approach will generate coronal equilibrium-like conditions.

6.2.1 The Newton-Raphson method

The eight extra equations (eq. 6.1, 6.2, 6.3 and 6.4) constitute a non-linear equation set. A correction to a guessed solution can be found based on the linearization of these equations. The corrected guessed solution then serves as the new guess and a new correction can be found. This procedure is known as Newton-Raphson iteration and its detailed description is given below.

For a set of n equations, $F_i(\mathbf{x}) = F_i(x_1, x_2 \dots x_n) = 0$, the linearization is just the first order Taylor polynomial about the guessed solution $\mathbf{x}_{(0)} = (x_1^{(0)}, x_2^{(0)} \dots x_n^{(0)})$,

$$\begin{aligned}
F_1(\mathbf{x}) &\approx F_1(\mathbf{x_{(0)}}) + \frac{\partial F_1}{\partial x_1}\delta x_1^{(0)} + \frac{\partial F_1}{\partial x_2}\delta x_2^{(0)} + \ldots + \frac{\partial F_1}{\partial x_n}\delta x_n^{(0)} \\
F_2(\mathbf{x}) &\approx F_2(\mathbf{x_{(0)}}) + \frac{\partial F_2}{\partial x_1}\delta x_1^{(0)} + \frac{\partial F_2}{\partial x_2}\delta x_2^{(0)} + \ldots + \frac{\partial F_2}{\partial x_n}\delta x_n^{(0)} \\
&\vdots \\
F_n(\mathbf{x}) &\approx F_n(\mathbf{x_{(0)}}) + \frac{\partial F_n}{\partial x_1}\delta x_1^{(0)} + \frac{\partial F_n}{\partial x_2}\delta x_2^{(0)} + \ldots + \frac{\partial F_n}{\partial x_n}\delta x_n^{(0)},
\end{aligned}$$

where $\delta x_i^{(0)} = (x_i - x_i^{(0)})$ are the absolute corrections. Since all of the equations have a zero right hand side, $F_i(\mathbf{x}) = 0$, the above equation set can be expressed as a matrix equation,

$$\left.\begin{pmatrix} \frac{\partial F_1}{\partial x_1} & \frac{\partial F_1}{\partial x_2} & \cdots & \frac{\partial F_1}{\partial x_n} \\ \frac{\partial F_2}{\partial x_1} & \frac{\partial F_2}{\partial x_2} & \cdots & \frac{\partial F_2}{\partial x_n} \\ \vdots & & \ddots & \\ \frac{\partial F_n}{\partial x_1} & \frac{\partial F_n}{\partial x_2} & \cdots & \frac{\partial F_n}{\partial x_n} \end{pmatrix}\right|_{\mathbf{x}_{(0)}} \begin{pmatrix} \delta x_1^{(0)} \\ \delta x_2^{(0)} \\ \vdots \\ \delta x_n^{(0)} \end{pmatrix} = - \begin{pmatrix} F_1(\mathbf{x}_{(0)}) \\ F_2(\mathbf{x}_{(0)}) \\ \vdots \\ F_n(\mathbf{x}_{(0)}) \end{pmatrix}.$$

Defining the derivative matrix as $\mathbf{J}_{(0)}$, the correction vector as $\delta\mathbf{x}_{(0)}$ and the function values on the right hand side as $-\mathbf{F}_{(0)}$, this matrix equation takes the simpler form,

$$\mathbf{J}_{(0)}\delta\mathbf{x}_{(0)} = -\mathbf{F}_{(0)}. \tag{6.5}$$

When dealing with very large and very small numbers, it is convenient and numerically more precise to work with relative changes. The equivalent

equation for the relative correction is

$$\begin{aligned}(\mathbf{J}_{(0)}\mathbf{X}_{(0)})(\mathbf{X}_{(0)}^{-1}\delta\mathbf{x}_{(0)}) &= -\mathbf{F}_{(0)} \\ \mathbf{J}'_{(0)}\delta\mathbf{x}'_{(0)} &= -\mathbf{F}_{(0)}, \end{aligned} \tag{6.6}$$

where

$$\mathbf{X}_{(0)} = \begin{pmatrix} x_1^{(0)} & 0 & \dots & 0 \\ 0 & x_2^{(0)} & \dots & 0 \\ \vdots & & \ddots & \\ 0 & 0 & \dots & x_n^{(0)} \end{pmatrix}. \tag{6.7}$$

Solving equation 6.6 provides the relative corrections, $\delta\mathbf{x}'_{(0)}$. Updating the guessed solution ($\mathbf{x}_{(0)}$) and repeating the above algorithm is likely to produce a smaller correction the second time. The solution to the original equation set, F_i, is found by repeating until convergence occurs, i.e. corrections drop below some defined maximum limit.

The update of the solution is an important step and typically is

$$x_i^{(j+1)} = x_i^{(j)}(1 + p\delta x_i'^{(j)}), \tag{6.8}$$

where p is a factor controlling the length of the Newton step $\delta x_i'^{(j)}$. Ideally $p = 1$ but sometimes it is useful to let $p < 1$ and a good choice is

$$p = \frac{1}{1 + d|\delta x_i'^{(j)}|}, \tag{6.9}$$

where d is a damping parameter. Setting $d = 0$ will allow for the full Newton correction, while $d > 0$ will decrease the corrections if they are large and have less of an impact when corrections are small. d is an input parameter in the code. Small values will generally give faster running code, but this comes at the cost of a higher risk of failed convergence. Simulations presented in section 7.3 were produced with $d = 5$.

The Newton-Raphson method requires the derivatives of all the equations that are to be solved (eq. 6.1, 6.2, 6.3 and 6.4). These are not listed here, but can be found in Leenaarts et al. (2007).

6.2.2 Algorithm

Bifrost advances its fundamental variables with a Hyman time stepper (Hyman, 1979) generalized to time steps of different lengths. This is a two step

process consisting of a prediction step followed by a correction step. The time stepping of the rate equations for the hydrogen is also done in two steps, but uses an Euler predictor corrector setup. The full algorithm of the time dependent hydrogen with the operator splitting then looks like this:

```
***********************************************
( .. fundamental variables predicted ... )

call get_fluxdivergence
! dndt contains the fluxdivergence
do i=1,6
  nsave(i) = n(i) + 0.5*dndt(i)*dt
  n(i) = n(i) + dndt(i)*dt
end do

call newtonraphson(e,r,dt)
call compute_pressure

( ... fundamental variables corrected ... )

call get_fluxdivergence
do i=1,6
  n(i) = nsave(i) + 0.5*dndt(i)*dt
end do

call newtonraphson(e,r,dt)
call compute_pressure
***********************************************
```

The arguments sent into the Newton-Raphson solver illustrates the equations dependency on these. The pressure is computed in the subroutine `compute_pressure` (eq. 2.31). The flux divergence is computed in two steps: first the flux and then the divergence. Due to the regular occurrence of extreme occupation number gradients, a basic first order upwind scheme is used to compute the flux. Second order spatial derivatives of this flux are used to compose the divergence.

6.3 Initial state of the time dependent non-LTE EOS

The time dependent non-LTE treatment of hydrogen described above, hereby referred to as the *Hion-package*, was implemented but it had yet to be tested

within the new framework of Bifrost. This new implementation was very similar to that of Bifrost's predecessor *Oslo Stagger Code* that had been tested in two dimensions and gave nice results (Leenaarts et al., 2007). The Newton-Raphson solver did initially not produce convergence, causing program execution to end.

6.3.1 Debugging

The reason for failure in the Newton-Raphson solver was an error in the interpolation routine for the collisional rate coefficients. Later it was also found that the pressure (needed for the equation of motion 2.28) was not being updated in the ghost-zones causing visibility of the sub-domain boundaries as discontinuities in the variables. The interpolation-fix enabled the program to advance some time steps, but convergence issues were still persisting. A self-inflicted error in a collisional rate coefficient derivative was the primary reason for the convergence failure and weird looking results (see fig. 6.2). The methods used to deal with failing convergence are described in section 6.4.

Another type of error revealed itself when the Newton-Raphson solver was stable enough to simulate a few minutes of solar time. Figure 6.3 displays the symptons, stripes and large cold unmoving chunks in the chromosphere. The solutions to this problem are discussed in section 6.5

6.4 Failed convergence

6.4.1 Averaging variables

The easiest way to deal with failed convergence is to accept and continue with a more or less appropriate set of variable values that do not necessarily have to satisfy the equations. Still it should contribute to a continuous feel in the variables' local distributions. One obvious choice is the average value of neighbouring points. It's possible to refine the method so that one or two average values are adjusted in order to enforce the satisfaction of one or two of the equations. Typically these are the highest occupation number and the electron density enforcing hydrogen nuclei conservation and charge conservation.

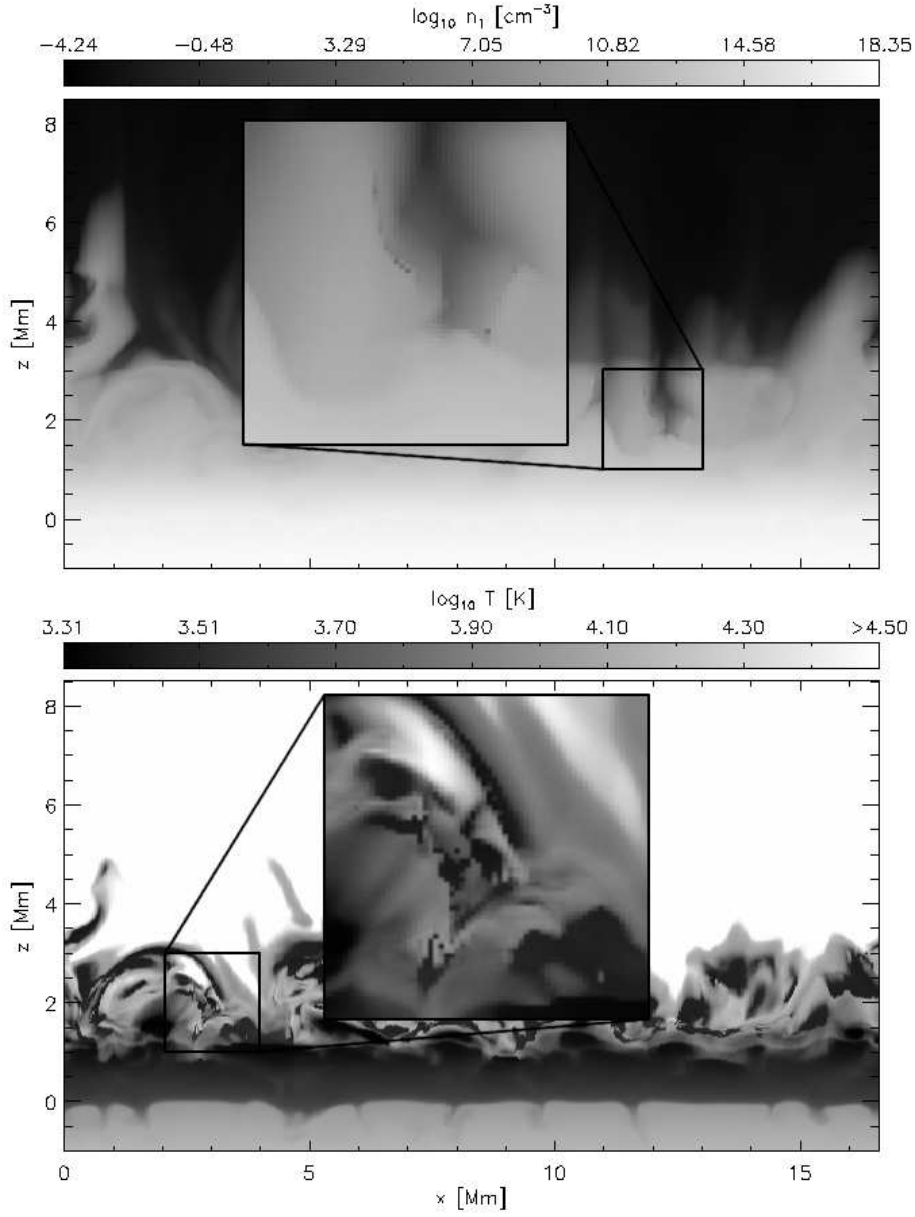

Figure 6.2: Illustration of error due to failed convergence. Number density of hydrogen ground state (upper panel) with a magnification of a region where the Newton-Raphson solver is about to fail. The black dots correspond to points that have converged to a wrong solution. These points would for the most part be taken care of by averaging variables, but new ones would pop up. Another problem was the discontinuous temperature structure (lower panel). The features that are magnified correspond to points and regions that had converged but clearly were erroneous due to their uneven appearance and lack of movement due to the ambient flow.

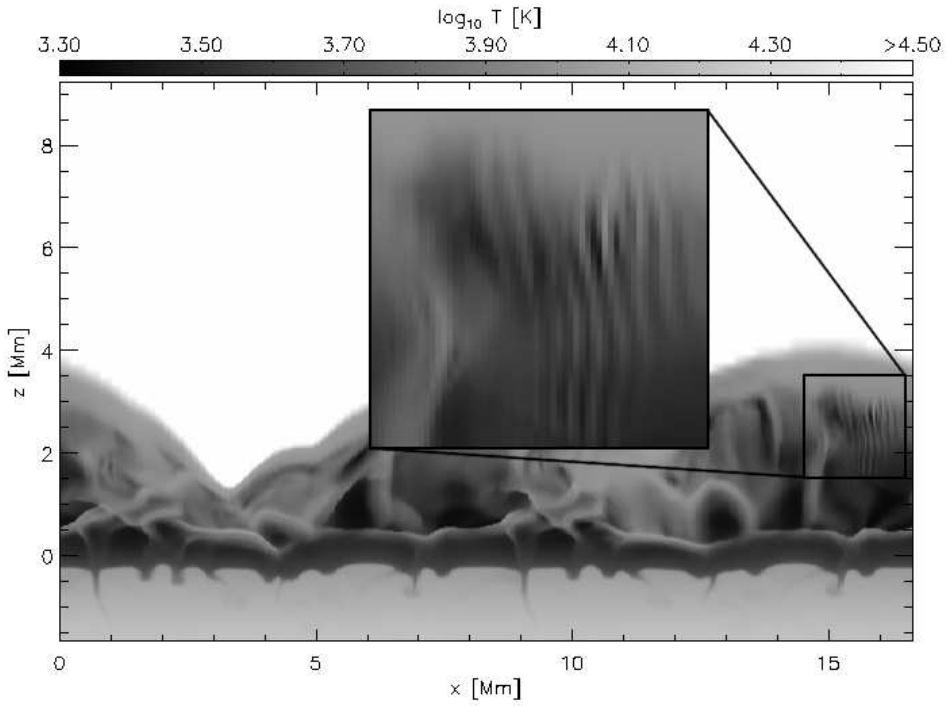

Figure 6.3: Illustration of error occurring after a few minutes of simulated solar time. Temperature with a zoom in on a problematic region: long lived stripe patterns are formed in the chromosphere. When they fade out, new ones develop elsewhere. Below the magnification is a cool region about to become fixed in space, confined by the very sharp edge around it from $x = 5.5$ Mm to $x = 9$ Mm.

6.4.2 Backtracking

Another way to deal with failed convergence is to let the factor p, controlling the length of the Newton step (eq. 6.9), be determined in a way that ensures the new solution, $\mathbf{x}_{(i+1)}$, to *always* provide a better fit to the equations, $\mathbf{F}(\mathbf{x}) = 0$. This method will be referred to as the *backtracking method*. A summary of the method is presented here. More information is found in Press et al. (1992).

The aim of the Newton-Raphson solver is to find a solution that satisfies $\mathbf{F}(\mathbf{x}) = 0$ as much as possible within the numeric limit. By defining

$$f = \frac{1}{2}\mathbf{F}^2, \tag{6.10}$$

this aim can be reformulated to satisfying $f = 0$ within this limit. The Newton step ($\delta\mathbf{x}$) is always orientated in a direction that reduces f:

$$\begin{aligned} \nabla f \cdot \delta\mathbf{x}' &= (\mathbf{F}^T\mathbf{J}')(-\left[\mathbf{J}'\right]^{-1}\mathbf{F}) \\ &= -\mathbf{F}^2 \leq 0. \end{aligned} \tag{6.11}$$

Although the initial rate of change of f is negative, it may become positive along the track of the Newton step since the equations are not linear. The full Newton step is in other words not guaranteed to decrease the value of f, but *small* steps in the Newton direction are. A successful Newton-Raphson iteration can be stated mathematically as follows:

$$\begin{aligned} f(\mathbf{x}_{(i+1)}) &< f(\mathbf{x}_{(i)}) \quad \text{where} \\ \mathbf{x}_{(i+1)} &= \mathbf{x}_{(i)}(1 + p\delta\mathbf{x}_{(i)}). \end{aligned} \tag{6.12}$$

The strategy is to use as large a p as possible for fast convergence. If it does not decrease f, a smaller Newton step is used, making sure f decreases before accepting the step. The criterion for accepting a step can not, however, be limited to the satisfaction of the above inequality (eq. 6.12), as convergence to a minimum of f might fail for two reasons. First, f may not decrease sufficiently relative to the step lengths, and second, step lengths could be too small relative to the initial rate of decrease of f. The second problem is solved simply by defining a minimum limit for p. The first problem is solved by requiring that the average rate of decrease of f must be a fraction α of the initial rate of decrease:

$$f(\mathbf{x}_{(i+1)}) \leq f(\mathbf{x}_i) - \alpha\nabla f \cdot (\mathbf{x}_{i+1} - \mathbf{x}_{(i)}). \tag{6.13}$$

A good value for α is 10^{-4} (Press et al., 1992).

After computing the corrections (eq. 6.6) the variables are ready to be updated. The first step length is usually $p_1 = 1$, but since the variables

are electron density, temperature and occupation numbers, all of which may never have a value less than 0, p_1 must in some cases be adjusted to ensure the absence of negative variable values. This is necessary only if relative changes are less than -1.

If the first step length, p_1, fails to satisfy eq. 6.13, backtracking commences. Let

$$\begin{aligned} g(p) &= f(\mathbf{x}(1+p\delta\mathbf{x})) \quad \text{so that} && (6.14)\\ g'(p) &= \nabla f \cdot \delta\mathbf{x}'. && (6.15) \end{aligned}$$

Now $g(p_1)$ is available together with $g(0)$ and $g'(0)$ (the latter of which is easily computed). This is enough information to model $g(p)$ as a quadratic polynomial,

$$\begin{aligned} g(p) &\approx ap^2+bp+c \quad \text{where} && (6.16)\\ a &= \left[g(p_1)-g'(0)p_1-g(0)\right]/p_1^2,\\ b &= g'(0) \quad \text{and}\\ c &= g(0). \end{aligned}$$

The p resulting in the smallest g is the solution to $g'(p)=0$,

$$p_2 = -\frac{g'(0)p_1^2}{2\left[g(1)-g'(0)p_1-g(0)\right]}. \tag{6.17}$$

If the criterion (eq. 6.13) is satisfied for p_2, the step is accepted and a new set of corrections is computed. If not, g is modeled as a cubic polynomial. Available now are $g(0)$, $g(p_2)$, $g(p_1)$ and $g'(0)$. The polynomial is

$$\begin{aligned} g(p) &\approx ap^3+bp^2+cp+d \quad \text{where} && (6.18)\\ \begin{pmatrix} a\\ b \end{pmatrix} &= \frac{1}{p_2-p_1}\begin{pmatrix} \frac{1}{p_2^2} & -\frac{1}{p_1^2}\\ -\frac{p_1}{p_2^2} & \frac{p_2}{p_1^2} \end{pmatrix}\begin{pmatrix} g(p_2)-g'(0)p_2-g(0)\\ g(p_1)-g'(0)p_1-g(0) \end{pmatrix}\\ c &= g'(0)\\ d &= g(0). \end{aligned}$$

The minimum p is the positive solution to the second order equation $g'(p)=0$:

$$p_{min} = \frac{-b+\sqrt{b^2-3ag'(0)}}{3a}. \tag{6.19}$$

If equation 6.13 is not yet fulfilled, a new cubic polynomial approximation is applied with the most recent information available on g. This process goes on until convergence occurs or p becomes smaller than the set minimum value. If it does, the backtracking is not successful.

6.4.3 Cutting the time step

A shorter time step will produce less change in the variables and hence give the Newton-Raphson solver an easier time converging the equation set. The time dependent equation of state couples to the mass density and energy density through the equations 6.2 and 6.3. These fundamental variables are made available in the time step cuts by linear interpolation.

Consider a cell not converging from the time t_i to the time $t_i + \Delta t$, where Δt is the time step length. The time step is cut into n_{cut} pieces so the Newton-Rapshon solver is set to work the intervals $(t_i,\ t_i + \Delta t/n_{cut})$, $(t_i + \Delta t/n_{cut},\ t_i + 2\Delta t/n_{cut}) \ldots (t_i + [n_{cut} - 1]\,\Delta t/n_{cut},\ t_i + \Delta t)$. When the Newton-Rapshon solver starts, the fundamental variables have already been determined. In order to get their previous value, backward first order integration is used,

$$\rho_{old} = \rho_{new} - \Delta t \frac{\partial \rho}{\partial t} \tag{6.20}$$

$$e_{i,old} = e_{i,new} - \Delta t \frac{\partial e_i}{\partial t}. \tag{6.21}$$

The setup is then:

```
deltat=dt/ncut
do i=1,ncut
  frac=i/ncut
  e_tmp=eold*(1.0-frac) + enew*frac
  r_tmp=rold*(1.0-frac) + rnew*frac
  call newtonraphson(e_tmp,r_tmp,deltat)
end do
```

6.5 Numeric noise

The stripes shown in figure 6.3 are caused by the numeric treatment in the solver. The equation representing the hydrogen nuclei conservation (eq. 6.3) replaces one of the rate equations. The rate equation removed is the one for the level with the highest valued occupation number. Since the terms in the discretized equation (eq. 6.4) are normalized by the occupation number, this choice represents the smallest throwaway of information due to the computer's finite real number precision.

However, by removing a level's rate equation, its occupation number is bounded by less restrictions. Generally the hydrogen nuclei conservation

equation is not satisfied when the Newton-Raphson solver starts, and the removed level's occupation number is the most likely candidate for change in order to gain satisfaction. The initial dissatisfaction of equation 6.3 has two reasons: first, the hydrogen is advected with a first order upwind setup while the mass density is treated by a fifth order interpolation sixth order derivative setup causing disproportional advection, and second, as temperature gets low, the formation of hydrogen molecules comes into play. Since the molecule formation is assumed to be in (instantaneous) LTE, the number density is may change a lot from one time step to the next. Ideally advection and a rate equation for the hydrogen should be solved. Now, for each ionized hydrogen atom added to satisfy equation 6.3, 13.6 eV are moved from the thermal energy term and placed in the ionization energy term, causing a decrease in temperature.

The stripes formed in places where the ionization degree was high and had a steep gradient.

6.5.1 Scaling the occupation numbers

By scaling the occupation numbers after the advection treatment, the discrepancy between them and the mass density is minimized causing less numeric noise. The scaling factor, c, is

$$c = \frac{A\rho}{\sum_i n_i + 2n_{H2}}, \tag{6.22}$$

where n_i are the advected occupation numbers. n_{H2} is the most recent molecule density and $A\rho$ is the total number density of hydrogen atoms.

6.5.2 Use all of the rate equations

By removing the hydrogen nuclei conservation equation and replacing it by the last rate equation, none of the occupation numbers are less bounded by restrictions (other than that of the numeric noise). This makes it likely that the adding and removing of protons is handled more balanced.

Applying all rate equations should only be done in regions with a high ionization degree and where its gradient is steep, which is where the stripes form).

6.5.3 Add extra heating term

By adding artificial heating if temperature goes below some predefined limit, the molecule formation problem can be avoided by simply setting the lowest allowed temperature high enough for molecule formation to be less potent. This will lead to less problems with the hydrogen nuclei conservation equation.

6.5.4 Diffusion

By smearing out the occupation numbers, the stripes would follow and be washed away faster than they would grow. The implementation is something like this:

```
call get_fluxdivergence
do i
  do j
    do k
      ntmp=sum(nold(i-1:i+1,j-1:j+1,k-1:k+1)-nold(i,j,k))/8.0
      n(i,j,k) = (1-a)*n(i,j,k) + a*ntmp + dndt(i,j,k)*dt
    end do
  end do
end do
```

where `a` is a parameter controlling the diffusion strength.

6.6 Hion modifications

All of the above methods to deal with problems have been tried out with varying levels of success. The scaling of the occupation numbers, which in some sense can be thought of as adding diffusion, removed very many stripes, but not all. By also adding the artificial heating term, setting the lowest allowed temperature to 2400 K, all discontinuity problems have vanished.

The direct diffusion (with scaling) worked too fast, and smeared out too much, even with very small `a`-values. Using all of the rate equations proved effective, but the loss of consistency between the mass density and hydrogen was not acceptable. In the worst cases, there would be 1.5 times more hydrogen than the density allowed.

Even though the program with these modifications run quite smoothly, the Newton-Raphson solver still fails to converge from time to time, forcing execution to a halt. When this happens the solver cuts the time step and tries again. If this fails, the solver will remove the hydrogen nuclei conservation equation and replace it with the last rate equation. If all of this fails, the variables are averaged and simulation continues. Most of the time cutting the time step is enough to give convergence. In 10-20% of the cases this is not enough and all rate equations are used. In about 1% of the cases the variables are averaged.

The backtracking method has not shown any success on failed convergence, and It is not recommended for further use.

6.7 Performance

6.7.1 The Hion package

The Hion-package introduces eight additional equations to the eight original MHD equations. These are non-linear and and their simultaneous solution is found with the Newton-Raphson method. As described in section 6.2.1, this requires the evaluation of eight functions (eq. 6.1, 6.2, 6.3 and 6.4), their derivatives with respect to all the involved variables and the inversion of an 8×8-matrix for every iteration in each cell.

The extra computing time introduced by the solver can roughly speaking be split into three equal parts. One third is spent on inverting the 8×8-matrix, one third is spent on evaluating the rate equations and their derivatives and the last third is spent on what's left (including advection, the last three equations, administration etc.). The matrix inversions are done with a gaussian elimination routine from the LAPACK[1]-package which means that there is probably not much to gain (in terms of efficiency) by editing it. The third representing the evaluation of the rate equations and their derivatives can again be split into three roughly equal parts: obtaining the collisional rate coefficients, obtaining the radiative rate coefficients and summing up the rates in the equations. The collisional rate coefficients are found with fifth order polynomial fits to values based on Johnson (1972). The evaluation of the radiative rate coefficients include a lot of unavoidable if-testing inside loops, due to the fixed/unfixed radiation temperature setup of the Sollum approximation. It was, however, found some efficiency gain potential in the last part. Summing up rates manually in loops, instead of by the use the intrinsic function `matmul`, decreased the extra Hion-time by about 5-10%.

[1] http://www.netlib.org/lapack/

Figure 6.4: Ghostzones that can be trusted after the different steps in the algorithm. Ghostzone with reliable values (light grey), ghostzone with unreliable values (dark grey) and subdomain (white). 1: Before prediction. 2: After prediction. 3: After correction.

The single most time consuming routine in the last third is the interpolation needed to obtain e_i^{noH}, n_e^{noH} and their derivatives. The default is a standard bilinear interpolation setup. In the Newton-Raphson solver, however, this interpolation routine provides values that are not always varying as smoothly as required to obtain convergence. When this happens, the solver starts over with a bicubic interpolation setup which costs a lot more, but provides smoothly changing variables.

6.7.2 Reducing communication

When high order spatial derivative setups are employed, the ghostzones values need to be updated after every step (here a step means either the prediction or the correction). Since there are five ghostzones and the Hion advection setup is of low order only, communication can be limited to after every correction step. Less communication comes at the cost of solving the Hion-equations in the innermost ghostzones after each prediction step. Figure 6.4 shows schematically in one dimension which of the ghostzones that can be trusted after each step of the algorithm. 1: Ghostzones just updated. 2: After the prediction step. It would have been possible to have three safe ghostzones instead of two, but that would only provide extra computing time and no gain. 3: After correction step only the subdomain cells contain reliable values and ghostzones must be updated before continuing with a new prediction step.

Less communication will be advantageous only if communication is slower than the Hion solver. Some communication must take place between the two steps, so the possible cpu time spent on waiting in MPI-calls for other cores (load imbalance) will in general not be reduced. The communication speed will depend on the machine on which the code is being run, and an

input parameter has been added to the code in order to easily be able to switch between the two communication setups. On both the local machines at ITA and on the Notur Hexagon system the most efficient way to run the code was found to be with communication after every step (see figure 6.5).

6.7.3 Speedtest

Figure 6.5 gives an impression on how the Hion-package performs on a varying number of cores. There is a discontinuity in both the upper and lower panels separating the two different machines used: the typical machine at the Institute of Theoretical Astrophysics (ITA, UiO) and the Notur Hexagon system. The upper panel shows the average time per simulated time step for Hion with full communication (solid), for Hion with reduced communication (dashed), for Hion with bicubic interpolation (see section 6.7.1) and full communication (dash-dotted), and finally the average time per time step with Hion switched off, using the equation of state lookup table (dotted). The Bifrost code without Hion runs about double as fast on Hexagon than on the ITA machines using 16 cores. Some improvement in performance is seen also with the Hion-package going from ITA machines to Hexagon, but not as much. Less communication does not increase speed for any number of cores on any of the machines tested. When using only bicubic interpolation, the average time per time step is doubled on Hexagon but only slightly increased on ITA's machines. The reason for this different behavior on the two types of machines is not known. Some of the explanation seem to lie in the bicubic interpolation routine's use of Fortran's intrinsic function `matmul`. Doing the matrix multiplication manually seem to improve performance, but not nearly enough to explain the large difference in the two interpolation methods.

The lower panel of figure 6.5 shows the efficiency number, defined as the average time per time step with the Hion-package switched on divided by the average time per time step with the equation of state lookup table (which is the dotted line in the upper panel). The line types correspond to the ones used in the upper panel. Here it becomes very clear that the efficiency loss due to bicubic interpolation on the ITA machines is very small compared to what is the case on Hexagon. Running the code with the Hion-package on a large number of cores will give the best efficiency. The test simulations used to produce figure 6.5 was done on a grid with $256\times128\times160$ points. When running on 160 cores (which is the maximum value in the figure), the cores have a subdomain with $32\times32\times32$ points each.

These measurements show that the optimum performance for the Hion-package is by running it on a large number of cores. The computing time

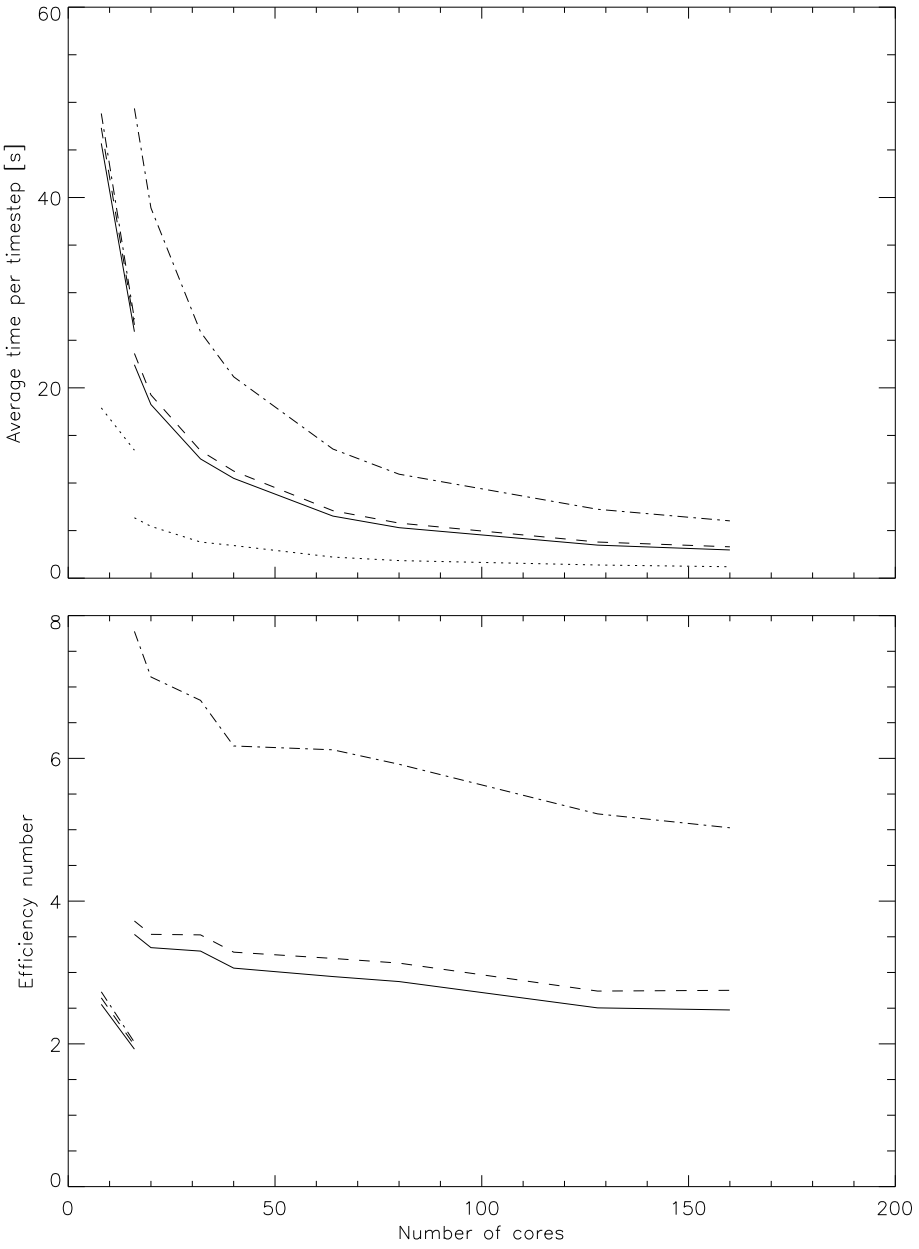

Figure 6.5: Upper panel: Average time per time step. Hion with full communication (solid), Hion with reduced communication (dashed), Hion with bicubic interpolation and full communication (dash-dotted) and without Hion (dotted). The discontinuity at 16 cores separate local machines at ITA from the Notur Hexagon system. Lower panel: Corresponding efficiency numbers, defined as Hion-time divided by the no-Hion time. Legends are the same as in the upper panel and again the discontinuity at 16 cores is due to the different machines on which the code was run in the test.

will be factor 2-3 higher than when the equation of state lookup table is used.

Part III

Numerical results

Chapter 7

Simulation results

7.1 Computing details

Two three-dimensional radiation magnetohydrodynamic simulations have been performed with the stellar atmosphere code Bifrost. Both simulations were carried out on Notur's Hexagon system which is a Cray XT4 distributed memory system that consists of 1388 quad-core nodes (for a total of 5552 cores) interconnected with a high-bandwidth low-latency switch network (SeaStar2).

The two simulations start from the same initial snapshot, but evolve somewhat differently as one of the simulations employs the LTE equation of state and the other employs the Hion equation of state.

The simulation box spans a region 16x8x15 Mm stretching from the convection zone to the corona distributed on 256x128x160 grid points. The points are equally distributed along the x-axis and y-axis with a point separation of 65 km. Along the z-axis more grid points are concentrated towards the lower parts of the atmosphere with a point separation of 32 km. Further up in the coronal regions of the atmosphere, where the physical phenomena typically has a larger spatial extent, less grid points are needed and the spacing is expanded to 440 km.

The LTE simulation covers 32 solar minutes and was done on 128 cores in 72 hours, which is equivalent to about 9200 cpu hours. The Hion simulation was significantly more expensive on the computational side. It covers 34 solar minutes and clocked in at 265 hours working on 160 cores. This is effectively about 42000 cpu hours. Table 7.1 contains more information about the simulations. The computing time per time step of the non-LTE

Simulation data		
EOS	LTE	Hion
Solar time [min]	32	34
Number of time steps	260000	190000
Number of cpus	128	160
Simulating time [h]	72	265
Cpu time [h]	9200	42000
Cpu time per timestep [s]	127	796

Table 7.1: Simulation data. Simulations carried out with the non-LTE equation of state produces more realistic results at a higher computational cost. In this case the non-LTE simulation time exceeded that of LTE by a factor 6.3.

simulation was a factor 6.3 larger than that of the LTE simulation (- the simulations were carried out before the discovery of the code's sensitivity to the choice of interpolation method, see figure 6.5).

7.2 Initial model

Both simulations start from the same initial state. The snapshot is in a state of dynamic equilibrium where the hydrogen ionization is taken to be in LTE. Figure 7.1 shows the mass density and temperature in four horizontal layers, $z = \{5.00, 2.04, 1.00, 0.20\}$ Mm. Figure 7.2 shows the degree of hydrogen ionization ($F_i = n_{HII}/(n_{HI} + n_{HII})$) and the electron density at the same heights.

The lower slice (0.20 Mm) corresponds to the photosphere. A vague granular pattern is visible in all the variables (at lower z it is more pronounced). All are fairly constant except for the hydrogen ionization degree which has a range of nearly 8 orders of magnitude. At $z = 1.00$ Mm this range is even larger, covering almost 15 orders of magnitude. The large range can be attributed to the exponential temperature dependence in the Saha equation (eq. 2.35). The electrons present at this height are coming from the metals, except for in the red spots where the hydrogen ionization level is high enough to dominate electron contribution (this happens approximately when $F_i > 10^{-4}$, see fig. 5.2).

Typical changes in the lower two heights are occurring on a sub-Mm length scale. Higher up in the atmosphere, changes increase their spatial extent. At $x = 6$ and $x = 13$ Mm a low density height temperature structure spans

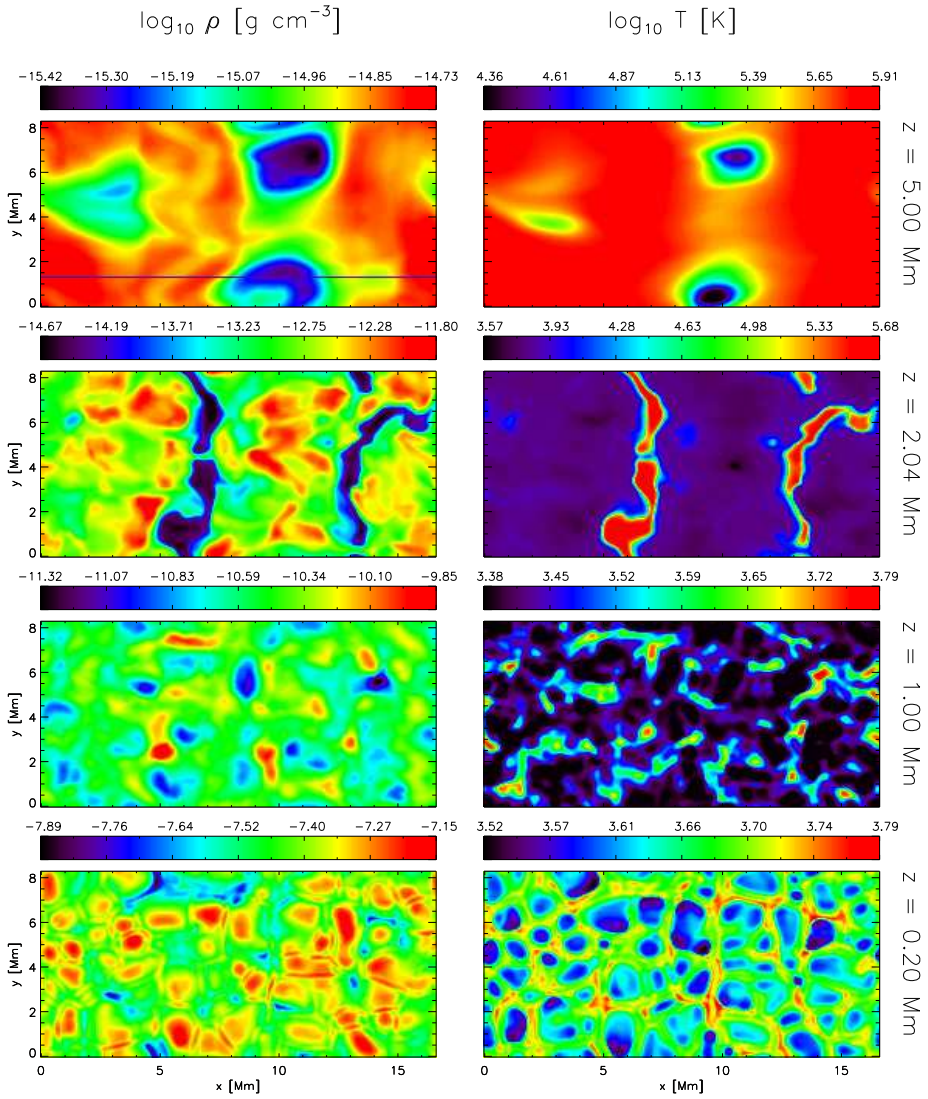

Figure 7.1: Mass density (ρ, left column) and temperature (T, right column) at four atmospheric heights. From top to bottom: $z = 5.00$ Mm, $z = 2.04$ Mm, $z = 1.00$ Mm and $z = 0.20$ Mm. The line in upper left panel ($y = 1.30$ Mm) indicates the position of the vertical slices displayed in figure 7.3.

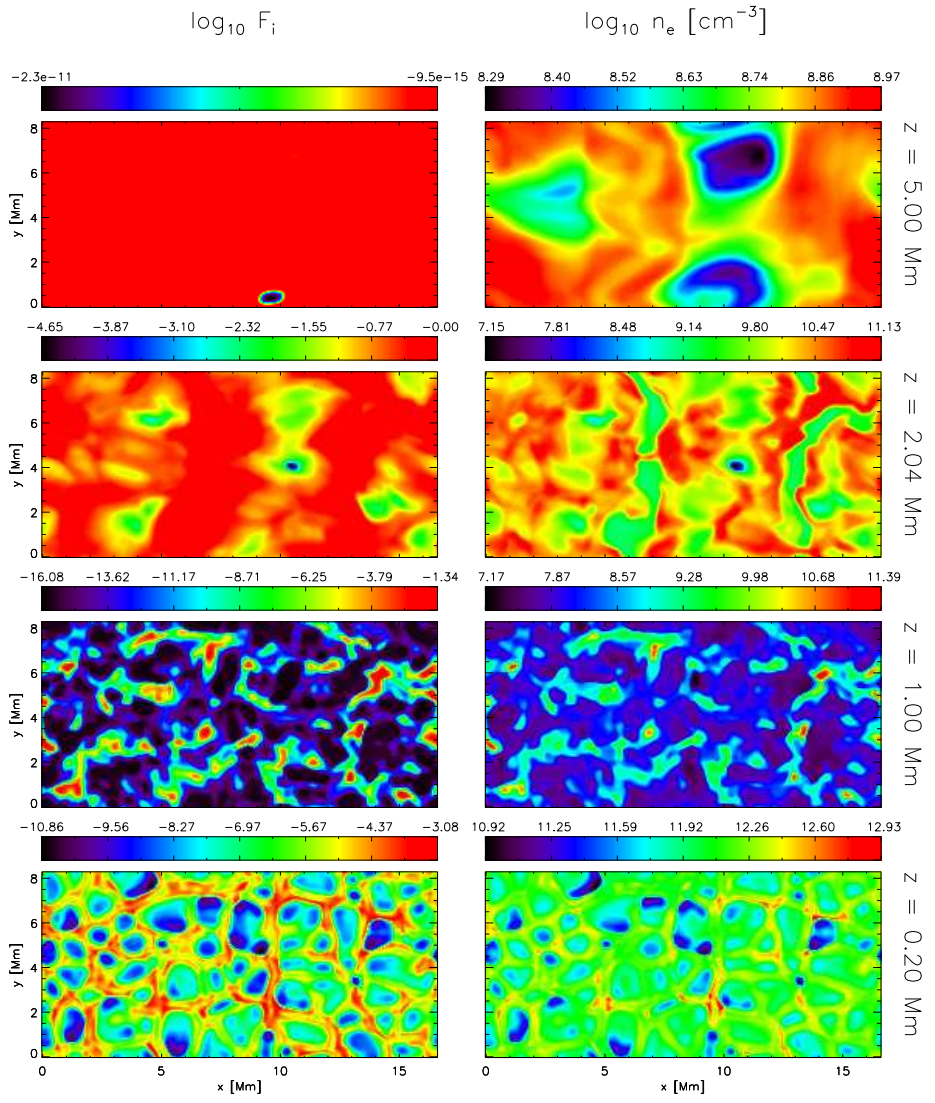

Figure 7.2: Degree of ionized atomic hydrogen ($F_i = n_{HII}/(n_{HI} + n_{HII})$, left column) and electron density (n_e, right column) at four atmospheric heights. From top to bottom: $z = 5.00$ Mm, $z = 2.04$ Mm, $z = 1.00$ Mm and $z = 0.62$ Mm.

the y-dimension. These are the foot points of a loop, visible in figure 7.3. The loop forms a tunnel parallel to the y axis.

In the tunnel top, the temperature is never below 23000 K. In such temperature regimes virtually all hydrogen and helium are ionized causing them to become the dominating electron donors (see fig. 5.1). Consequently every gram of mass contributes with the same amount of electrons and as a result the electron density is proportional to the mass density.

7.3 Results

7.3.1 Time evolution of the two simulation runs

Figure 7.4 displays the time evolution of the (top to bottom) hydrogen ionization degree, temperature and electron density in the column $(x, y) = (13.0, 6.5)$ Mm for both simulation runs (non-LTE: left, LTE: right). Other columns have been looked at and the thermodynamic behaviour is similar. Figure 7.5 display the time evolution of the same variables, but this time in a horizontal row located at $(y, z) = (1.30, 1.45)$ Mm. At this height the differences between the two simulation runs really stand out.

Already after the first shock has passed the time dependent hydrogen ionization level seems to have found its dynamic equilibrium or relaxed state. The system as a whole seems to reach such a state only after about 15 minutes entering a somewhat more chaotic phase especially visible in the temperature structure.

From the height-time plots it is clear that the hydrogen ionization degree is deviating from its LTE value in the chromosphere, while the LTE treatment seems to be a good approximation to photospheric and coronal conditions. LTE ionization levels adjust instantly to local changes of energy density causing large temporal variations over a scale of a few minutes. Hydrogen is ionized in the shocks propagating through the atmosphere and recombines between them as energy density decrease. In the non-LTE run recombination happens on finite timescales long enough for hydrogen to remain ionized even between the shocks.

As a result of the higher and less varying level of hydrogen ionization (which means small variations in the ionization energy), the temperature will have an increased sensitivity to changes in the energy density. This is seen in figures 7.4 and 7.5 where the temperature in the non-LTE case fluctuates

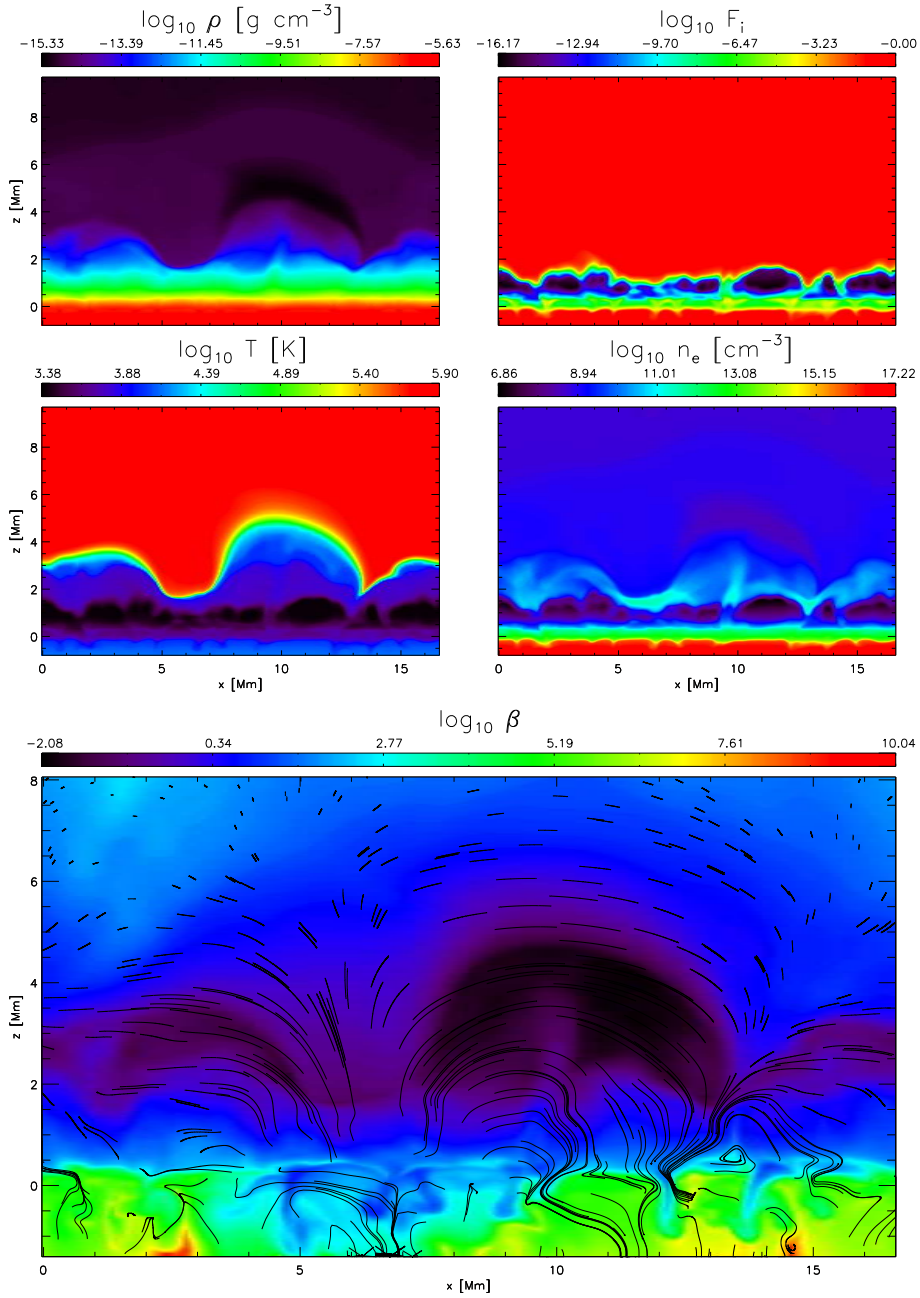

Figure 7.3: Clockwise from top left: mass density, degree of hydrogen ionization, electron density, plasma beta and temperature. All panels display the same vertical slice of the initial model ($y = 1.30$ Mm, indicated on upper left panel of fig. 7.1). The over-plotted arrows in the plasma beta panel indicates the direction and magnitude (proportional to arrow length) of the magnetic field projected onto the vertical slice.

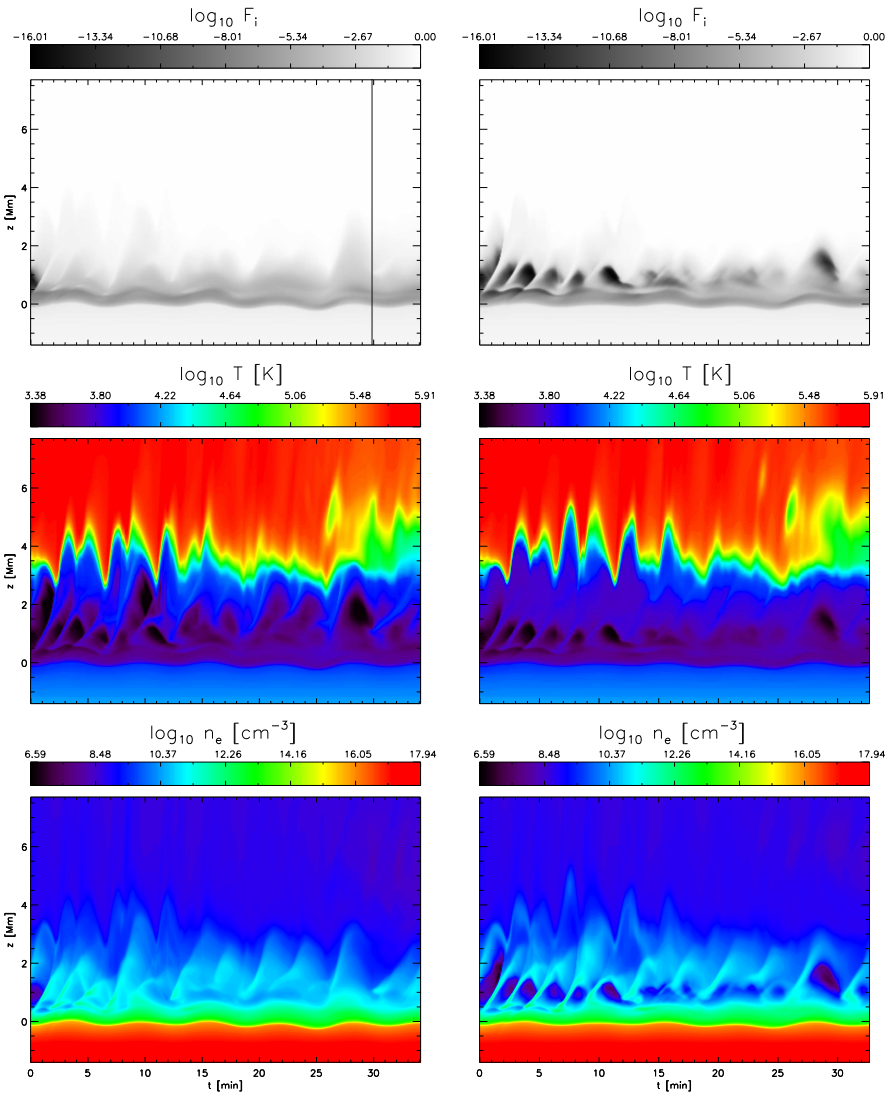

Figure 7.4: Time evolution of atomic hydrogen ionization degree (top),temperature (middle) and electron density (bottom) for non-LTE (left) and LTE (right) equation of state. Evolution is shown in the vertical column $(x, y) = (13.0, 6.5)$ Mm and the color scale is adjusted to span identical ranges for a variable's two panels. Large scale features and dynamics are similar in the two runs. Major differences are seen in the chromosphere where the hydrogen ionization level, in the non-LTE run, is found to be approximately constant while adjusting on an infinitely small timescale in the LTE run causing larger fluctuations.

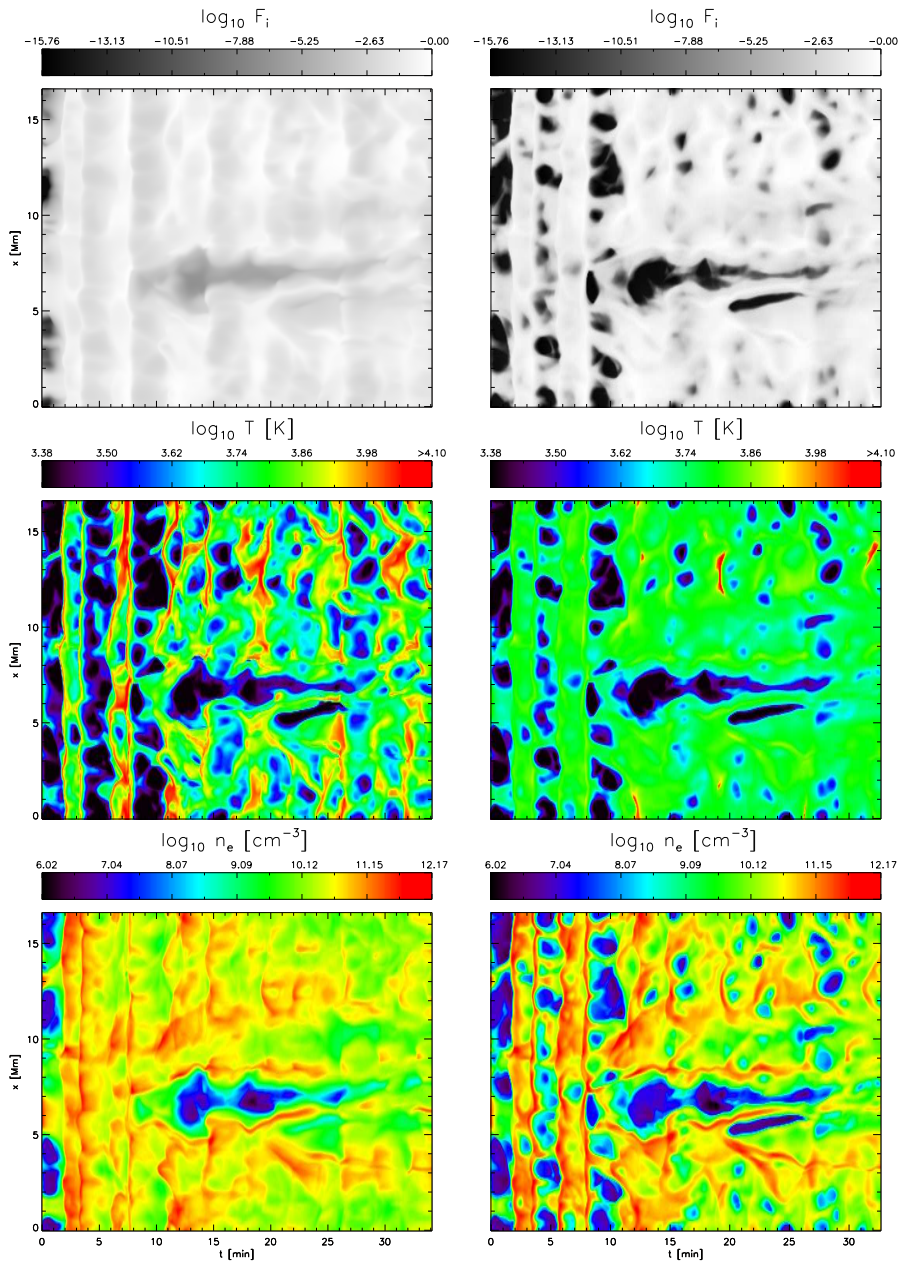

Figure 7.5: Time evolution of atomic hydrogen ionization degree (top),temperature (middle) and electron density (bottom) for non-LTE (left) and LTE (right) equation of state. Evolution is shown in the horizontal column $(y, z) = (1.30, 1.45)$ Mm and the color scale is adjusted to span identical ranges for a variable's two panels. Large scale features and dynamics are similar in the two runs. Less change in ionization levels result in large temperature variations and small electron density variations in the non-LTE run. In the LTE run large changes in the ionization levels result in small temperature variations and large electron density variations.

more than in the LTE case giving more small structures and larger variations. Generally it is true to say that energy density changes in the non-LTE run will alter the temperature while keeping the ionization levels more constant. The opposite is true in the LTE case where ionization levels fluctuate while temperature is kept stable. This was also pointed out by Leenaarts et al. (2007).

Electron densities in the chromosphere follow the hydrogen ionization degree as hydrogen is the dominant electron contributor. Less fluctuations are present in the non-LTE run than in the LTE run as the ionization level variations are smaller. The two runs have similar electron densities in the shock fronts since the equilibration time, τ_e (see section 2.4.1), here is becoming small enough for local conditions to determine the ionization state. Physically this corresponds to gas compressing and increasing the importance of the collisional transition rates. Between the shocks electron densities are sustained in the non-LTE run and decrease due to recombination in the LTE run.

7.3.2 At 25 minutes

The mass density at various heights after 25 minutes of solar time is shown in figure 7.6. The left column holds the result obtained from the non-LTE run and the right column values are obtained from the LTE run. The two runs have produced similar densities and most structures (especially those that are of large scale) are common and can be identified in both runs. This is consistent with what was found in section 7.3.1 with the large scale features developed in both simulation runs. There are still some differences, and inspection of the photospheric oscillations in figure 7.4 (wave form at $z \approx 0$ Mm) shows exactly four periods after 25 minutes in the non-LTE run and slightly above 4 periods in LTE-run. This gives the impression of the LTE-obtained densities as being slightly more developed than non-LTE densities. Viscosity coefficients were adjusted during the simulation and this may very well be the cause of the small difference in period. It is less likely that the non-LTE treatment of the hydrogen would give this effect as the oscillations are driven from the convective motions below the photosphere - a region where LTE is a good approximation (fig. 7.4).

The hydrogen ionization degree at heights $z = 3.96$ Mm, $z = 2.04$ Mm, 1.00 Mm and $z = 0.20$ Mm is shown in figure 7.7. The left column displays values obtained from the non-LTE run and the right column displays the values obtained from LTE relations consistent with the mass density and internal energy from the non-LTE run. Note that the color scales are adjusted to display differences better.

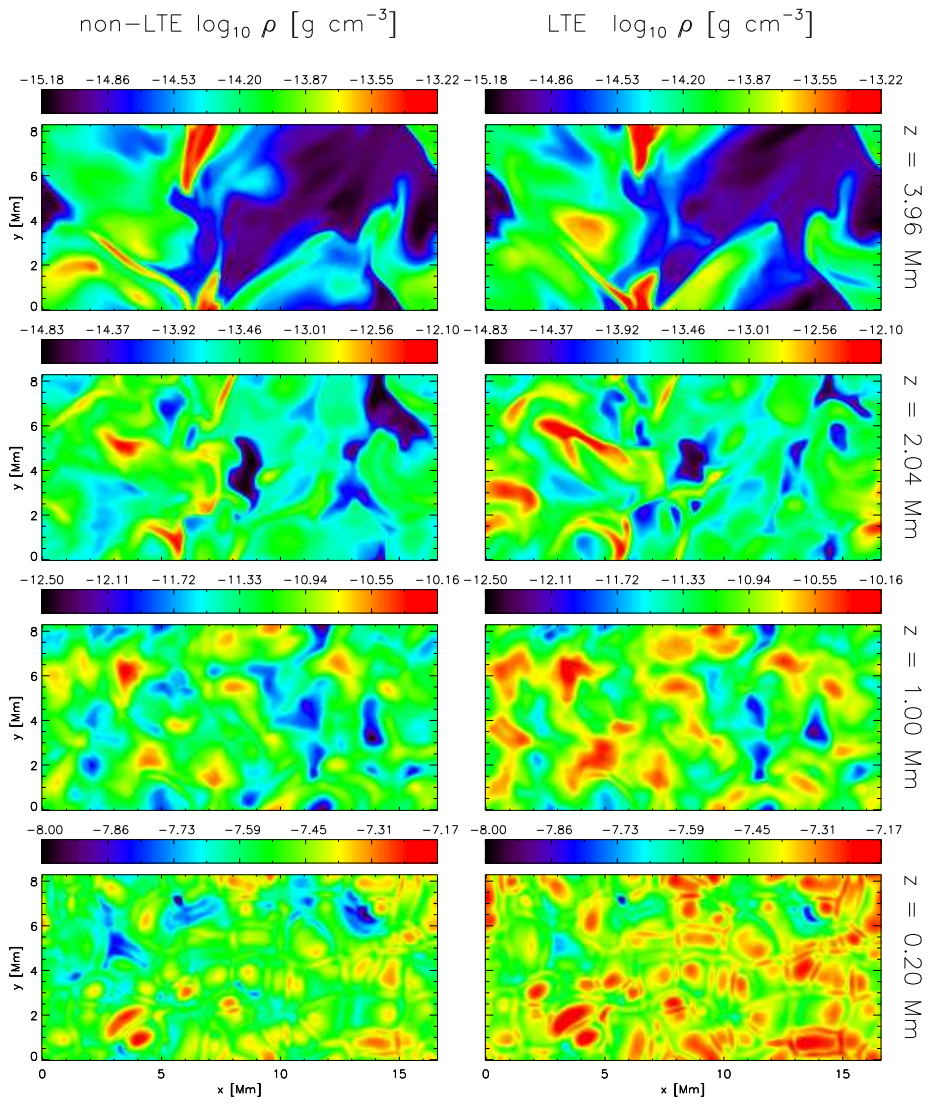

Figure 7.6: Mass density for the non-LTE run (left) and the LTE run (right) after 25 minutes of solar time at heights from top to bottom: $z = 3.96$ Mm, $z = 2.04$ Mm, $z = 1.00$ Mm and $z = 0.20$ Mm. The color scale is adjusted to span an equal range for the two runs at each height. The two runs have not evolved identically, but semi-large and large scale features (such as in the two upper panels) are very similar. Also the vague granular patterns are the same.

Hydrogen ionization levels are not found to be in LTE in any of the featured heights. In the $z = 3.96$ Mm slice the ionization degree varies from about 40% to 100%. Temperatures are large (see fig. 7.8) and the instantaneous ionization level is generally higher than predicted by the non-LTE run.

At height $z = 2.04$ Mm structures are very similar except for the two dark spots at $x = 7$ Mm where the non-LTE hydrogen ionization degree is about ten orders of magnitude higher than the corresponding LTE value. It is not easy to read it off the figure itself, but by numeric inspection it is found that the LTE ionization degree on average (at $z = 2.04$ Mm) is 21% higher than the corresponding non-LTE values. At the next height, $z = 1.00$ Mm, deviations from LTE are easily spotted, with LTE values spanning about ten orders of magnitude more than the non-LTE values. Some features are common while others are only found in the LTE values. The $z = 0.20$ Mm panels both show granular patterns. Again the LTE values show greater variation than those of non-LTE. However, the differences are here occurring in a range where hydrogen plays an insignificant role both as an electron donor and in the energy balance (eq. 2.32) and as such the electron density and temperature will be very near their LTE values.

Figures 7.8 and 7.9 show for both non-LTE and LTE the temperature and electron density, respectively, at the four heights $z = 3.96$ Mm, $z = 2.04$ Mm, $z = 1.00$ Mm and $z = 0.20$ Mm. The left columns display the values obtained from the non-LTE simulation run and the right columns display the values obtained from LTE relations consistent with the mass density and internal energy from the non-LTE run.

The non-LTE temperature is generally higher than that of LTE except in the $z = 0.20$ Mm layer. A lot more structure is present in the non-LTE values. The upper chromosphere (corresponding to the blue parts of the $z = 3.96$ Mm layer) has a temperature of about 8000-10 000 K. The LTE value is about 6000 K. In the corona (corresponding to the red parts of the upper panels) temperature rises to a few hundred thousand degrees. Here hydrogen is completely ionized leading to a match in the non-LTE and LTE values. The same qualitative (and quantitative!) behaviour is found in the $z = 2.04$ panels with the exception that there is far less coronal gas present at this height. At $z = 1.00$ Mm small temperature fluctuations are present. These are due to instabilities propagating through the atmospheric layer that have not yet been washed out or become large scale. The low temperature fluctuations are indicated also in the LTE temperature while the high temperature ones only appear with non-LTE treatment. The electron density in the high slice show the same structure in both non-LTE and LTE but it is on average about 5% greater in LTE. This is because of instantaneous ionization in the high temperature regions. At $z = 2.04$ Mm much of the

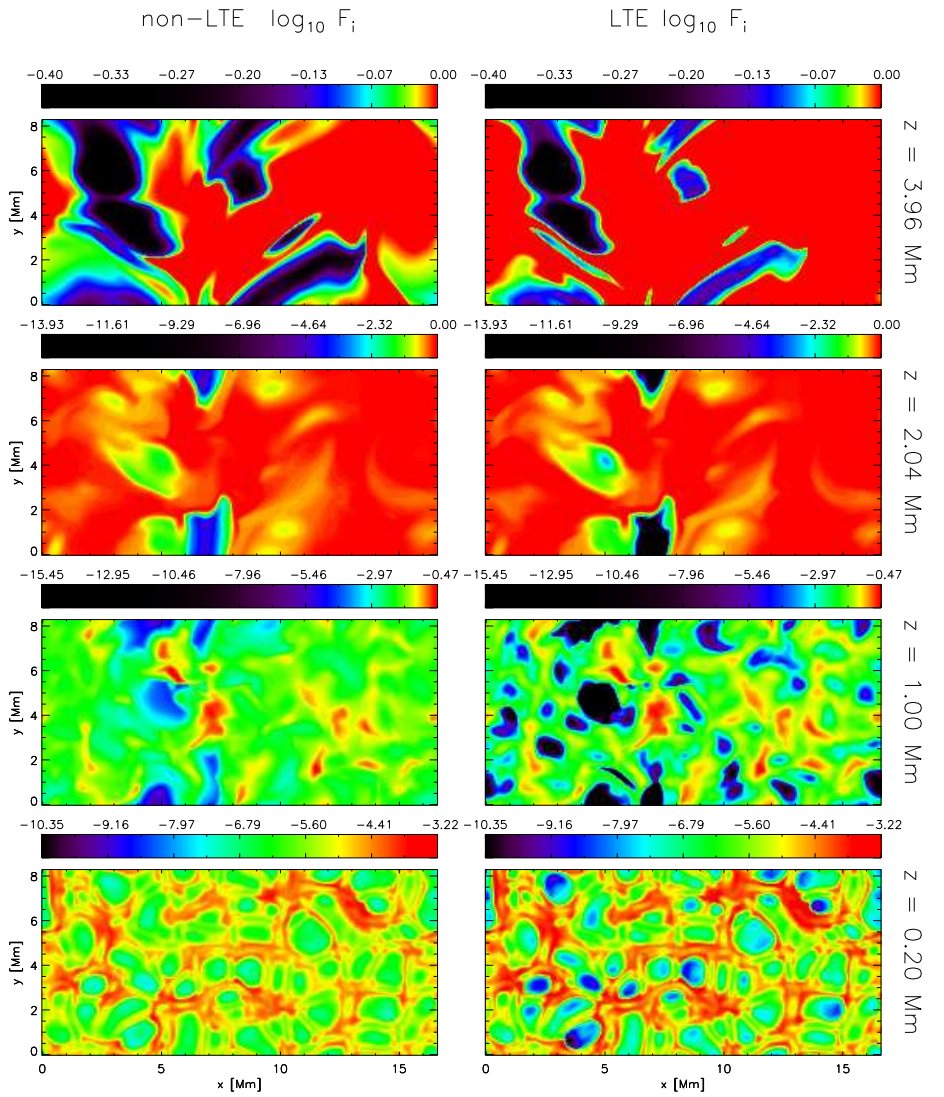

Figure 7.7: Ionization degree obtained from the non-LTE simulation run (left column) and the LTE values obtained from the mass density and internal energy from the same (non-LTE) snapshot (right column) after 25 minutes of solar time at various heights: $z = 3.96$ Mm, $z = 2.04$ Mm, $z = 1.00$ Mm and $z = 0.20$ Mm. The color scale is adjusted to span an equal range at each height. Note that the scale in the three upper rows is concentrated to the higher values. In none of the heights is hydrogen ionization levels in LTE but it is fairly near in the regions corresponding to photospheric and coronal conditions.

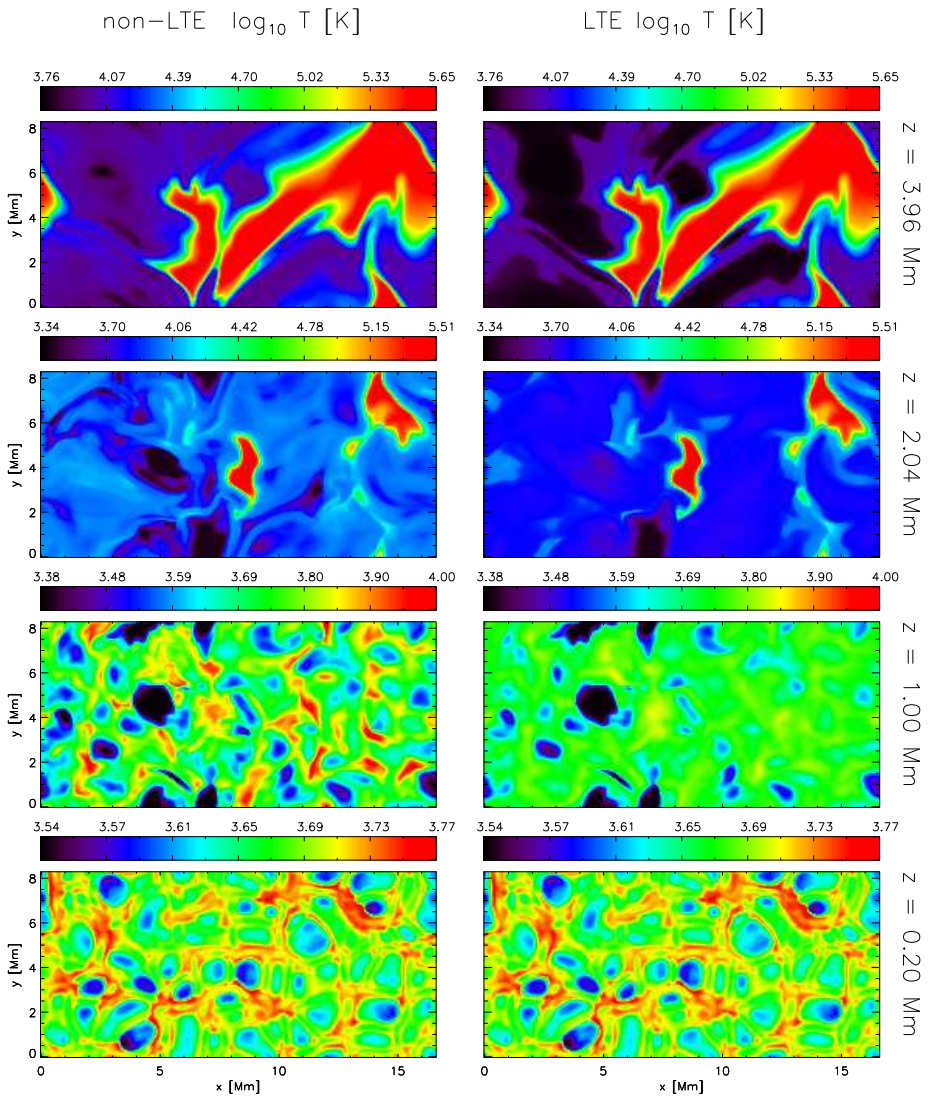

Figure 7.8: Temperature after 25 minutes of solar time. Values obtained from the non-LTE simulation run (left column) and LTE values consistent with the mass density and internal energy from the non-LTE run (right column) at the four heights: $z = 3.96$ Mm, $z = 2.04$ Mm, $z = 1.00$ Mm and $z = 0.20$ Mm. The color scale is consistent for each height. Only in the lowermost slice is LTE seen to be a precise approximation.

same is true. The non-LTE ionization level is lower than it is in LTE causing a lower electron density. This difference is particularly pronounced in the local temperature maxima. An important non-LTE correction is shown at $y = 6$ where electron density is about ten times higher than in LTE. At $z = 1.00$ Mm the non-LTE electron density show a smoother and less extreme behaviour than that of LTE due to the temperature sensitivity of the LTE approximation. In the $z = 0.20$ Mm layer the density is high enough for collisions to dominate particle interactions, which gives good agreement between non-LTE and LTE.

7.3.3 General picture

Figure 7.10 sums up the overall result. An instability has has developed into a shock and is propagating up through the atmosphere. Some of the energy the shock is carrying goes into ionizing hydrogen, and some goes into the thermal energy, increasing the temperature. The increase in ionization also results in an increase in the electron density.

LTE values are shown in dotted lines. They show that the energy that is being transported by the shock will much rather go into ionizing the material than it will increase temperature (which has a smooth variation), if local conditions were to decide. Behind and in front of the shock the ionization degree drops below time dependent values due to instantaneous adjustment to the local conditions, also visible in the electron density. In the upper chromosphere below the transition region the extra internal energy is spent on keeping the ionization level high, preventing a temperature rise. When there is no more hydrogen left to ionize and nowhere to store the internal energy, temperature quickly rise to coronal values where time dependent and instantaneous local values unite.

This difference in shock structure in LTE and non-LTE resembles that of Carlsson & Stein (1992) where an exact treatment of the hydrogen radiation transfer was employed.

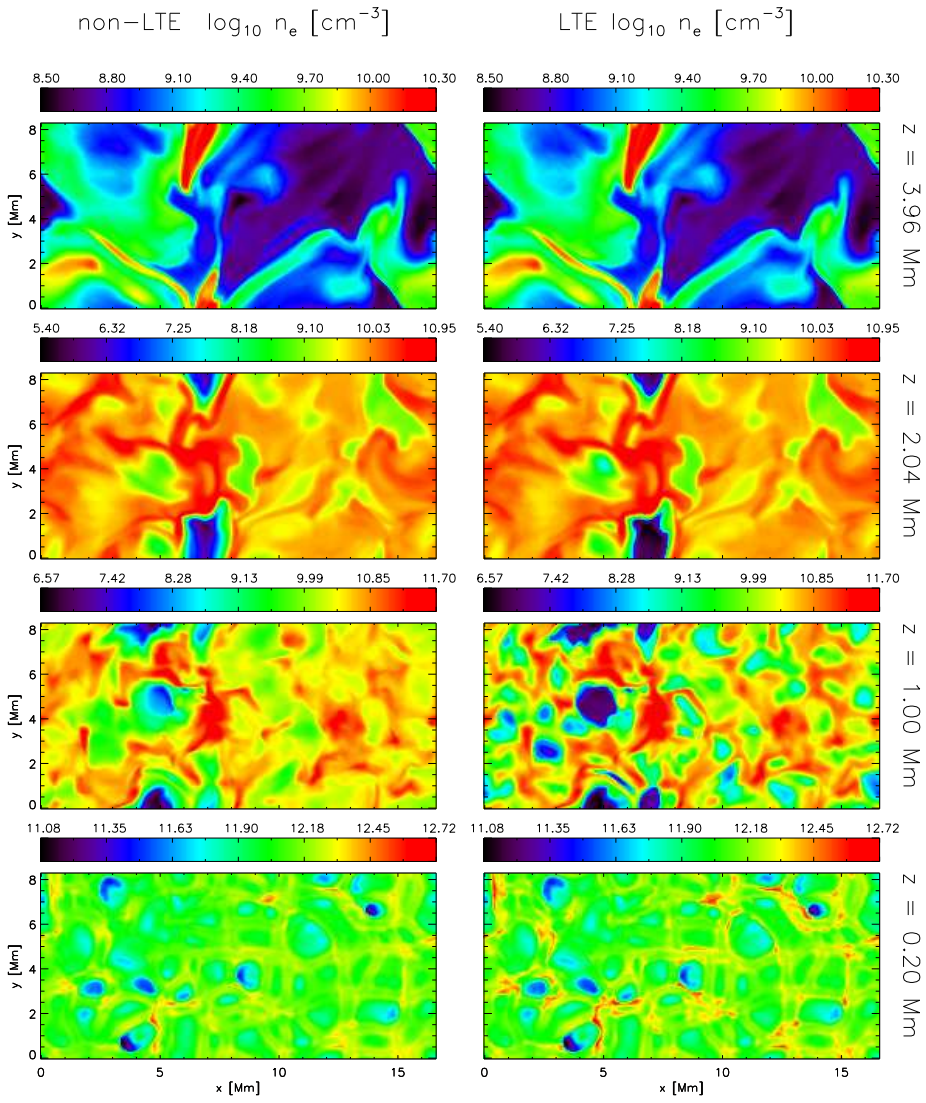

Figure 7.9: Electron density after 25 minutes of solar time. Values obtained from the non-LTE simulation run (left column) and the LTE values consistent with the mass density and internal energy from the same run (right column) at the four heights: $z = 3.96$ Mm, $z = 2.04$ Mm, $z = 1.00$ Mm and $z = 0.20$ Mm. The color scale is consistent for each height. Differences between non-LTE and LTE values follow the ionization degree (fig. 7.7).

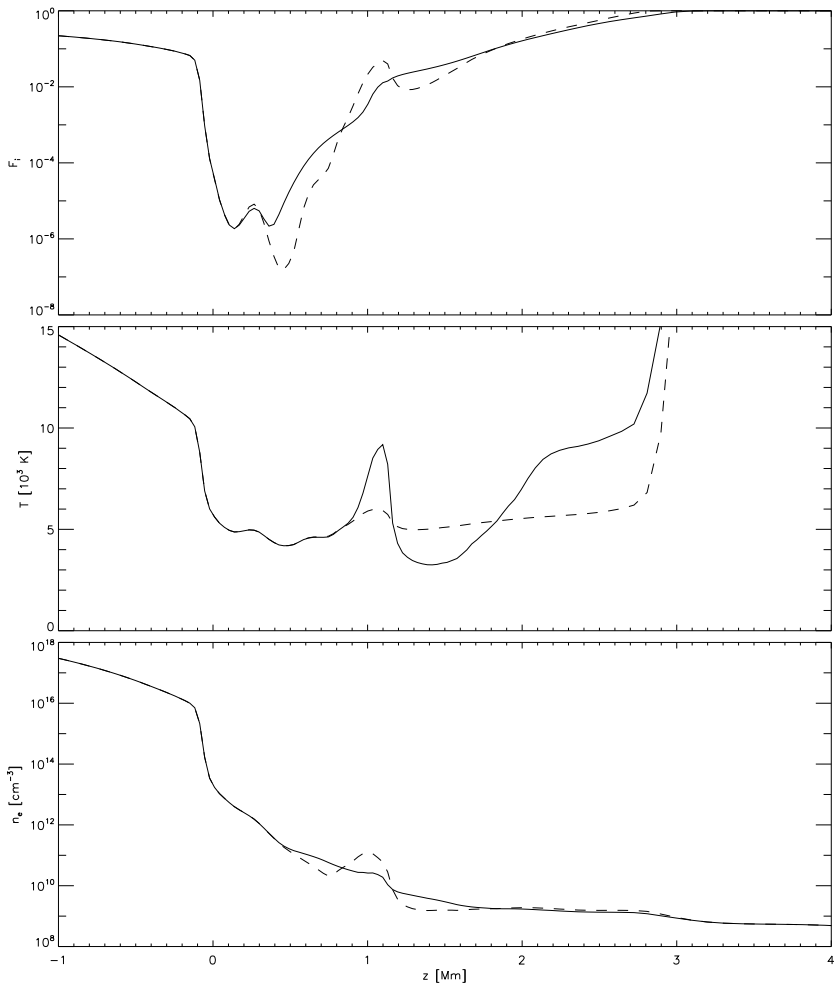

Figure 7.10: Hydrogen ionization degree (upper panel), temperature (middle panel) and electron density (lower panel) after 29 minutes and 50 seconds. Curves indicate non-LTE values (solid) and LTE values consistent with the mass density and internal energy from the non-LTE simulation run (dashed).

Chapter 8

Conclusion and outlook

The Bifrost code now contains a functional time dependent non-LTE hydrogen solver, providing a more realistic equation of state than the standard precomputed LTE table. This added realism comes at a high, but reasonable computational cost (a factor 2-3 more than with the precomputed LTE lookup table). The solver has been tested and is found to provide results consistent with earlier work (Carlsson & Stein, 2002; Leenaarts et al., 2007). Due to long time scales for ionization and recombination of hydrogen, its ionization degree will differ significantly from LTE values in chromospheric regions. Here, hydrogen dominates the equation of state and this leads to larger temperature fluctuations and smaller electron density fluctuations than predicted by LTE. The large scale dynamics are found to be less sensitive to the choice of equation of state.

8.1 Shortcomings

8.1.1 The Sollum-approximation

The radiative transfer of the Sollum-approximation was developed in a one-dimensional setting and its use in three-dimensional simulations might not be very accurate. The Sollum-approximation also assumes all Lyman transitions to be in detailed radiative balance. This is true up until just below the transition region, so the results here may very well be off.

8.1.2 Radiative energy flux divergence

The radiative heating term in the energy equation is based on matter in LTE, reading opacities and scattering coefficients from a table based on the mass and energy density. The more accurate temperature and electron densities from the Hion simulation should be employed as lookup variables to improve the realism of the radiative transfer. More electrons in Hion simulation may give more H^--heating that might give way for a reduction in the use of the artificial heating term (section 6.5.3) in the cool pockets of the simulation.

8.2 Future work

In the study of the chromosphere, results from simulations carried out with the realistic equation of state are interesting, as their temperature and electron density structures (generally not predictable by assuming LTE), enable for production of improved synthetic spectra of chromospheric lines. Figure 8.1 shows an observation of Hα which is such a line. A lot of structure is visible here that is not yet being reproduced in synthetic spectra.

The direct use of the occupation numbers from an Hion simulation to compute the emergent Hα intensity would not show any structure at all as the occupation numbers were computed by assuming the emergent intensity to be constant. Figure 1 of Leenaarts (2010) shows the statistical equilibrium vertically emergent Hα line core intensity computed from the non-equilibrium temperature and electron density from the two-dimensional simulation presented in Leenaarts et al. (2007). The intensity shows a granular pattern with superimposed shockwave structure. This is not consistent with observations where the granulation patterns in general do not show (figure 8.1).

Whether or not the third dimension in the Hion simulations has significance must be determined by solving the statistical equilibrium also for new results (such as those presented in chapter 7). The statistical equilibrium assumption may in itself be erroneous. It would be better to solve the time dependent radiative transfer problem assuming hydrogen to be a minority species, based on a time series of state variables from an Hion simulation (where of course the hydrogen is treated as a *majority* species). In addition to improvements of the already mentioned shortcomings, these are problems that should be addressed in the future.

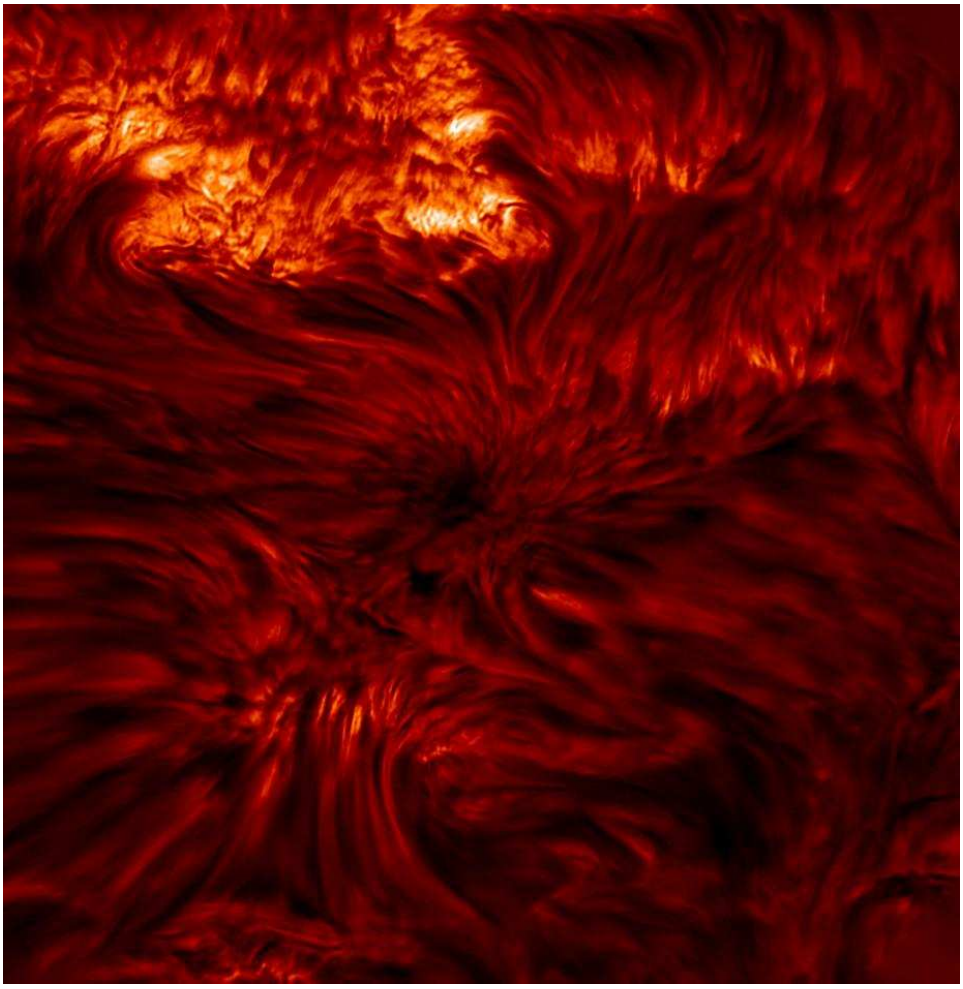

Figure 8.1: Hα image. Observed June 11th 2008 with with the CRisp Imaging SpectroPolarimeter (CRISP) instrument on the Swedish 1-m Solar Telescope (SST). The field of view is 66.6x68.3 arcseconds and there is a lot of filamentary structure as well as a small sunspot in the middle.

Bibliography

Cardona, O., Martínez-Arroyo, M., & López-Castillo, M. A.: 2010, "Atomic Partition Function for Stellar Atmospheres and Plasma Diagnostics", *Astrophys. J.* **711**, 239–245

Carlsson, M. & Stein, R. F.: 1992, "Non-LTE radiating acoustic shocks and CA II K2V bright points", *Astrophys. J.* **397**, L59–L62

Carlsson, M. & Stein, R. F.: 1995, "Does a nonmagnetic solar chromosphere exist?", *Astrophys. J. Lett.* **440**, L29–L32

Carlsson, M. & Stein, R. F.: 1997, "Formation of Solar Calcium H and K Bright Grains", *Astrophys. J.* **481**, 500–+

Carlsson, M. & Stein, R. F.: 2002, "Dynamic Hydrogen Ionization", *Astrophys. J.* **572**, 626–635

Cunto, W., Mendoza, C., Ochsenbein, F., & Zeippen, C. J.: 1993, "Topbase at the CDS", *Astron. Astrophys.* **275**, L5+

Grevesse, N. & Sauval, A. J.: 1998, "Standard Solar Composition", *Space Science Reviews* **85**, 161–174

Griffiths, D. J.: 1995, *Introduction to quantum mechanics*

Gudiksen, B. V., Carlsson, M., Hansteen, V., Hayek, W., Leenaarts, J., & Martínez-Sykora, J.: 2010, "The stellar atmosphere simulation code BIFROST", *Astron. Astrophys., in preparation*

Hansteen, V. H., Carlsson, M., & Gudiksen, B.: 2007, "3D Numerical Models of the Chromosphere, Transition Region, and Corona", in P. Heinzel, I. Dorotovič, & R. J. Rutten (Ed.), *The Physics of Chromospheric Plasmas*, Vol. 368 of *Astronomical Society of the Pacific Conference Series*, 107–+

Hayek, W.: 2008, "First 3D radiative transfer with scattering for domain-decomposed MHD simulations", *Phys. Scripta.* **133(1)**, 014006–+

Hyman, J. M.: 1979, "A method of lines approach to the numerical solution of conservation laws", in *Proceedings of the third IMACS international symposium on computer methods for partial differential equations*, Vol. 3

Johnson, L. C.: 1972, "Approximations for Collisional and Radiative Transition Rates in Atomic Hydrogen", *Astrophys. J.* **174**, 227

Leenaarts, J.: 2010, "Numerical simulations of the quiet chromosphere", *ArXiv e-prints*

Leenaarts, J., Carlsson, M., Hansteen, V., & Rutten, R. J.: 2007, "Non-equilibrium hydrogen ionization in 2D simulations of the solar atmosphere", *Astron. Astrophys.* **473**, 625–632

Leenaarts, J. & Wedemeyer-Böhm, S.: 2006, "Time-dependent hydrogen ionisation in 3D simulations of the solar chromosphere. Methods and first results", *Astron. Astrophys.* **460**, 301–307

Mihalas, D.: 1978, *Stellar atmospheres /2nd edition/*

Mihalas, D. & Mihalas, B. W.: 1984, *Foundations of radiation hydrodynamics*

Nordlund, A.: 1982, "Numerical simulations of the solar granulation. I - Basic equations and methods", *Astron. Astrophys.* **107**, 1–10

Press, W. H., Teukolsky, S. A., Vetterling, W. T., & Flannery, B. P.: 1992, *Numerical recipes in FORTRAN. The art of scientific computing*

Rutten, R. J.: 2003, *Radiation Transfer in Stellar Atmospheres*

Rybicki, G. B. & Lightman, A. P.: 1986, *Radiative Processes in Astrophysics*

Shu, F. H.: 1991, *Physics of Astrophysics, Volume I: Radiation*, University Science Books

Shu, F. H.: 1992, *The physics of astrophysics. Volume II: Gas dynamics.*, University Science Books

Skartlien, R.: 2000, "A Multigroup Method for Radiation with Scattering in Three-Dimensional Hydrodynamic Simulations", *Astrophys. J.* **536**, 465–480

Sollum, E.: 1999, *Hydrogen Ionization in the Solar Atmosphere: Exact and Simplified Treatments*

Spitzer, L. H.: 1967, *Physics of Fully Ionized Gases*

Thompson, K. W.: 1987, "Time dependent boundary conditions for hyperbolic systems", *J. Comput. Phys.* **68**, 1–24

Thompson, K. W.: 1990, "Time-dependent boundary conditions for hyperbolic systems. II", *J. Comput. Phys.* **89**, 439–461

Tsuji, T.: 1973, "Molecular abundances in stellar atmospheres. II.", *Astron. Astrophys.* **23**, 411–431

Vardya, M. S.: 1965, "Thermodynamics of a solar composition gaseous mixture", *Mon. Not. R. Astron. Soc.* **129**, 205–+

Vernazza, J. E., Avrett, E. H., & Loeser, R.: 1981, "Structure of the solar chromosphere. III - Models of the EUV brightness components of the quiet-sun", *Astrophys. J. Suppl. S.* **45**, 635–725

Wedemeyer, S., Freytag, B., Steffen, M., Ludwig, H., & Holweger, H.: 2004, "Numerical simulation of the three-dimensional structure and dynamics of the non-magnetic solar chromosphere", *Astron. Astrophys.* **414**, 1121–1137